Multiscale Computational Modeling of Nanofluidic Transport

by

Mengyi Wang

SUBMITTED TO THE DEPARTMENT OF MATERIALS SCIENCE AND ENGINEERING
IN PARTIAL FULFILLMENT OF THE REQUIREMENTS FOR THE DEGREE OF

MASTER OF SCIENCE IN MATERIALS SCIENCE AND ENGINEERING
AT THE
MASSACHUSETTS INSTITUTE OF TECHNOLOGY

SEPTEMBER 2020

Author _____
Mengyi Wang
Department of Materials Science and Engineering
June 30, 2020

Certified by _____
Heather J. Kulik
Associate Professor, Department of Chemical Engineering
Thesis Supervisor

Certified by _____
Jeffrey C. Grossman
Professor, Department of Materials Science and Engineering
Thesis Reader

Accepted by _____
Frances M. Ross
Professor, Department of Materials Science and Engineering
Chair, Departmental Committee on Graduate Studies

Multiscale Computational Modeling of Nanofluidic Transport

by

Mengyi Wang

Submitted to the Department of Materials Science and Engineering on June 30, 2020

in partial fulfillment of the requirements for the degree of

Master of Science in Materials Science and Engineering

Abstract

Water scarcity is one of the largest global challenges, affecting two-thirds of the world population. Water desalination and purification technologies, such as novel membrane processes and materials, are in great demand to produce clean water from contaminated sources or the sea. However, the lack of fundamental understanding of structure-property-performance has hindered the advancement of these techniques. In this study, we address this critical knowledge gap by adapting multiscale computational modeling to better understand the mechanisms of intrinsic molecular interaction in nanofluidic applications. We performed *ab initio* molecular dynamics to study the nanoscale solvation behavior of selected ions on finite graphene models. The degree of charge transfer between ion and water, and the effect of defects on dynamics and solvation has been investigated. Furthermore, a quantum mechanics/molecular mechanics (QM/MM) model for the accurate description of free energy changes in ion adsorption process has been developed. Lastly, we combined classical molecular dynamics and density functional theory (DFT) to elucidate the dielectric-driven mechanism of ionization behavior in nanoporous polyamide films. We seek to utilize this knowledge for the design of next-generation membranes for separation and water purification.

Thesis Supervisor: Heather J. Kulik
Title: Associate Professor of Chemical Engineering

Table of Contents

List of Figures

Fig. 5.3.1. Molecular dynamics simulations of the dielectric constant of bulk SPC/E water ranging from system sizes of 64 to 5832 water molecules.

Fig. 5.3.2 Calculated dielectric constants of confined water in potential walls of diameter 1~5 nm.

Fig 5.3.3 Relation between the pK_a of a polyamide-based R-COOH analogue (3,5-dicarbamoylbenzoic acid) and the dielectric constant of the surrounding media determined by density functional theory.

Fig. 5.3.4 Binding enthalpies between a polyamide-based piperazine analogue, acetylated-PIP (Ace-PIP), and probe anions gathered from DFT calculations.

Fig. 5.3.5 Role of media dielectric constant, determined by DFT, on the pK_a of Ace-PIP.

List of Tables

Chapter 1

Introduction

Nanofluidics[1], [2] is the study of fluid motion in a structure with dimension less than 100 nm in one or more dimensions. At this scale, fluids behave quite differently from the bulk and cannot be described with the continuum hydrodynamic laws of bulk fluids. The high surface-to-volume ratio, non-negligible surface charges and overlapping electric double layer in nanochannels and nanopores lead to capillarity-induced negative pressure in water[3], fast flows[4] and surface charge-governed ion transport[5]. Recent development of new nanofabrication techniques[6], [7] has enabled the design of novel devices in both energy and bio-related fields, e.g. in membrane science[8], biosensing[9] and nanofluidic electronics[10].

Fluidic transport at nanoscale

The transport of solvent and solute in nanofluidic devices is mainly affected by three factors: the presence of external driving forces (e.g. electrical potential or pressure gradients), the presence of colloidal forces (e.g. electrostatic forces, van der Waals and hydrophobic interaction) and the presence of frictional wall-fluid forces[1]. Almost all wall materials carry some kind of surface charge, leading to either attractive or repulsive colloidal interaction between wall and solute that act over short to long distances, and thus a solute concentration gradient across nanochannel. For example, in a system consisting charged solute ions and negative wall charge, due to the combined effect of electrostatic interaction and Brownian thermal motion, an electrical

double layer adjacent to the wall is formed (Fig 1.1[1]), and the resultant electrical potential in the double layer decays exponentially. Van del Waals forces have the longest range of all colloidal forces, whereas hydrophobic interaction is mainly dominant in short distances.

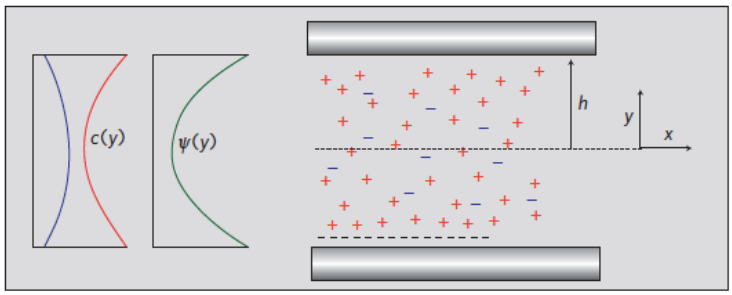

Fig 1.1 Solute concentration profile and total electrostatic potential in a nanochannel with positive (red) and negative (blue) ions. The walls are negatively charged. (Adapted from Ref[1])

In nanochannels, solvent transport can happen from pressure gradient (hydrodynamic flow) and/or electrical potential gradient (electro-osmotic flow)[1]. The average solvent velocity $\langle v_S \rangle$ can be calculated by

$$\langle v_S \rangle = \frac{1}{h}\int_0^h v_S(y)\,dy = \frac{1}{h}\int_0^h \underbrace{\left(\frac{1}{2\eta}\left(y^2 - 2hy\right)\frac{dP}{dx}\right)}_{\text{Hydrodynamic flow}} dy \quad + \frac{1}{h}\int_0^h \underbrace{\left(\frac{\varepsilon}{\eta}\left(\zeta - \psi(y)\right)\frac{d\phi}{dx}\right)}_{\text{Electro-osmotic flow}} dy$$

where 2h is the nanochannel width, ξ is the electrical potential at the plane of shear and ψ(y) is the electrical potential in the double layer, η is the solution viscosity and ε is the permittivity. In case of hydrophobic wall, the water density profile near the wall is low, therefore the water-wall interactions decrease and water could "slip" past the wall with 20-50 nm slip length[11], which increases both hydrodynamic and electro-osmotic flow. On the other hand, solute can be transported via solvent transport (convection), solute concentration gradient (diffusion) or ion

electrical potential gradient (migration). The area-averaged solute flux <J> under three driving forces is given by the Nernst-Planck equation:

$$\langle J\rangle = \frac{1}{h}\int_0^h \underbrace{(c(y)v_S(y))}_{\text{Convection}}\mathrm{d}y - \frac{1}{h}\int_0^h \underbrace{\left(D_\infty \frac{\mathrm{d}c(y)}{\mathrm{d}x}\right)}_{\text{Diffusion}}\mathrm{d}y - \frac{1}{h}\int_0^h \underbrace{\left(\frac{zqD_\infty}{kT}c(y)\frac{\mathrm{d}\phi}{\mathrm{d}x}\right)}_{\text{Migration}}\mathrm{d}y$$

where D_∞ is the diffusion coefficent in free solution and zq is the ionic charge. To account for frictional solute-wall interactions, these terms are usually modified by a hinderance factor that has been derived for a few solute and channel geometries[12].

Applications in materials science: example of carbon nanotube

Carbon nanotubes (CNT) are interesting candidates for nanofluidic applications because of their small pore sizes, rigid nonpolar structure and smooth hydrophobic surfaces, leading to frictionless water flow and fast transport that is orders of magnitudes higher than other conventional pores. Hummer *et al.* has used molecular dynamics (MD) simulations to study the spontaneous and continuous filling of a (6,6) nonpolar nanotube with water[4]. It has been reported that water rapidly filled the empty cavity of carbon nanotube via pulse-like transmissions and the filled state continued over entire simulation time of 66 ns[4]. Water inside the nanotube has lost two out of four hydrogen bonds on average and forms a one-dimensionally quasi-ordered chain along the nanotube, which is highly reminiscent of water chains observed in biological channels. On average, the measured water flux is around 51 x 10^{-14} cm^3 s^{-1}, on the same magnitude as water flow in long channels of transmembrane protein aquaporin-1[13]. Such continuous and rapid flow is enabled by high energy cost of water chain rupture and minimal interaction with the hydrophobic wall. Further simulations with reduced carbon-water attractions

(Fig 1.2(b)) resulted in emptying of CNT nanotube, suggesting tunable conductivity by changes in local channel polarity and solvent conditions[4].

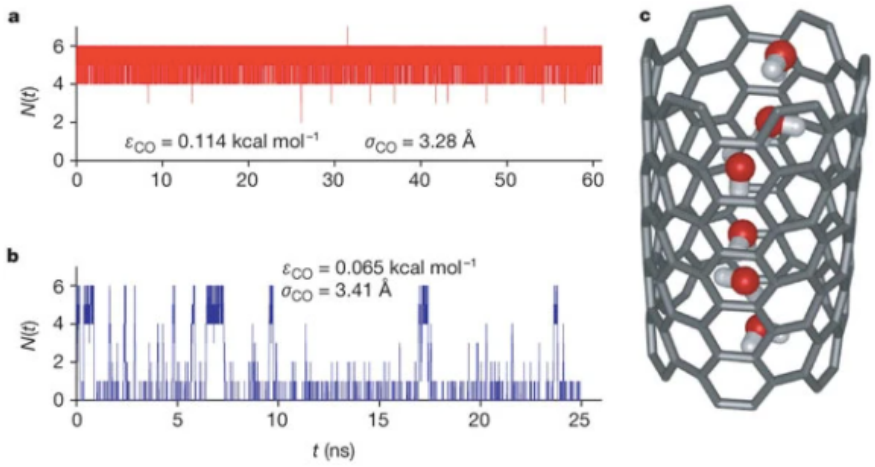

Fig. 1.2 Number of water molecules inside the nanotube as a function of time for (a) sp^2 carbon parameters and (b) reduced carbon-water attractions. (c) Structure of the hydrogen-bonded water chain inside the nanotube (Adapted from Ref[4]).

Several experimental and computational studies have demonstrated the applicability of chemically tunable CNT membranes as nanofiltration materials. For the entrance of small ionic species, such as Na^+, K^+, and Cl^- into uncharged tubes, size-based exclusion requires the diameter of CNT to be at least ~0.4 nm, comparable to the hydrated ion size. In this case, crossing the membrane requires the ion to lose part of its hydration shell, which is associated with a large energy barrier. As an example of size exclusion, Hinds' group has reported that biotin-functionalized-CNT-based membranes coordinated with streptavidin facilitates a reduction in ion flux by a factor of 24[14], highlighting their potential applications in controlled chemical separations or ion-channel mimetic sensors. Moreover, preferential transport can be induced by chemical modification of CNT. It is also possible to control solute transport by engineering the wall-solute interactions, e.g. changing the strength of electrolyte.

Carbon nanotubes are also used in nanofluidic field-effect transistors (Fig. 1.3[15]). In such devices, the flow through nanochannel can be controlled by pressure, applied electric field or concentration difference. By applying a bias voltage between the gate electrode and solution, the wall potential can be changed, modulating the counter-ionic charge in the solution[1]. Pang *et al.* has built a device where a narrow single-walled CNT of a few micrometers in length connects two fluid reservoirs[16]. The excess charge carried in the electrolyte results in very large electroosmotic currents due to nearly frictionless flow of water. Measurements of voltage-driven electrolytes flow reveals that ion currents are approximately 2 orders of magnitude higher than predicted from the bulk resistivity of the electrolyte, also the ion current has a unique power-law dependence $G \approx C^b$ on electrolyte concentration whereas other types of ion-channels (e.g. silicon based) typically have approximately constant conductance at low concentration and becomes proportional to concentration beyond C > 0.1 M[16]. The power law exponent is sensitive to the electrical properties of CNT, and the change of slope indicates b is probably affected by the total charges on CNT.

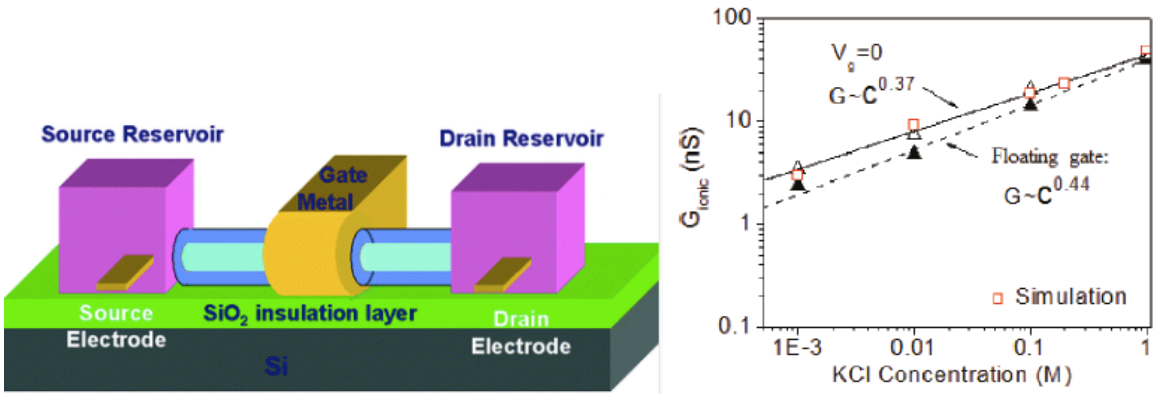

Fig 1.3 (a) Schematic of a nanofluidic field-effect transistor. (b) Concentration dependence of ionic conductance on salt concentration (Adapted from Ref[15], [16]).

Overview

In this thesis, we present three computational case studies in nanofluidics that scales from a few molecules to relatively bulk systems. Chapter 2 reviews the basic formalism behind density functional theory (DFT) and classical molecular dynamics (MD), two computational methods that we used to model the nanofluidic behavior in the following chapters. Chapter 3 uses *ab initio* MD to investigate the nanoscale solvation behavior and the intrinsic interaction between ions, water and graphene using a finite coronene model as an example. The influence of topological and chemical defects on the solvation has also been analyzed. Chapter 4 focuses on the development of a quantum mechanical/molecular mechanical (QM/MM) model to study ion adsorption to graphene, which serves as a basis for a more accurate description of change in free energy that takes into account many-body polarizations and long-range electrostatic interactions. Chapter 5 utilizes classical MD combined with first principle simulations to study the dielectric-driven mechanism of location-dependent ionization of carboxyl groups in polyamide membranes.

Chapter 2

Theory of methodology

Density functional theory[17], [18] (DFT), a computational quantum mechanical modeling method, has been one of the most promising techniques to compute the electronic structure of materials. It has been widely applied to predict a variety of properties at the atomic scale, such as molecular structure[19], vibrational frequencies[20], reaction thermochemistry[21], and magnetism[22]. Classical molecular dynamics[23], on the other hand, determines the trajectory of atoms and molecules using molecular mechanical force fields. It is extremely helpful in providing information of the dynamics of system, such as crystal nucleation[24] and ligand binding[25]. In this chapter, we will review the basic mathematical and physical formalism behind both of the techniques.

Density Functional Theory

The energy of a collection of atoms may be computed by solving the time-independent Schrödinger equation

$$\hat{H}\Psi_i(\vec{x}_1, \vec{x}_2, ..., \vec{x}_N, \vec{R}_1, \vec{R}_2, ..., \vec{R}_M) = E_i\Psi_i(\vec{x}_1, \vec{x}_2, ..., \vec{x}_N, \vec{R}_1, \vec{R}_2, ..., \vec{R}_M)$$

where H represents the Hamiltonian of a system consisting M nuclei and N electrons. The Hamiltonian can be written as

$$\hat{H} = -\frac{1}{2}\sum_{i=1}^{N}\nabla_i^2 - \frac{1}{2}\sum_{A=1}^{M}\frac{1}{M_A}\nabla_A^2 - \sum_{i=1}^{N}\sum_{A=1}^{M}\frac{Z_A}{r_{iA}} + \sum_{i=1}^{N}\sum_{j>i}^{N}\frac{1}{r_{ij}} + \sum_{A=1}^{M}\sum_{B>A}^{M}\frac{Z_A Z_B}{R_{AB}}$$

where the first two terms represent the kinetic energy of electrons and nuclei, and the remaining terms describe the attractive/repulsive electrostatic interactions between the nuclei and electrons. Since the nuclei move much slower than the electrons due to their heavy mass, according to the Born-Oppenheimer approximation, we can assume the electrons move in the field of fixed nuclei, and the electronic Hamiltonian can be simplified to

$$\hat{H}_{elec} = -\frac{1}{2}\sum_{i=1}^{N}\nabla_i^2 - \sum_{i=1}^{N}\sum_{A=1}^{M}\frac{Z_A}{r_{iA}} + \sum_{i=1}^{N}\sum_{j>i}^{N}\frac{1}{r_{ij}} = \hat{T} + \hat{V}_{Ne} + \hat{V}_{ee}$$

and average total energy for a specific state Ψ, i.e. the expected value of the energy, can be calculated by

$$E[\Psi] = \frac{\langle\Psi|\hat{H}|\Psi\rangle}{\langle\Psi|\Psi\rangle} \text{ where } \langle\Psi|\hat{H}|\Psi\rangle = \int \Psi^*\hat{H}\Psi d\vec{x}$$

According to the variance principle, the energy computed from a guessed state Ψ is an upper bound to the true ground state energy E_0. By taking minimization of $E[\Psi]$ with all possible many-electron wavefunctions, one can obtain the ground state wavefunction Ψ_0 and the associated energy $E[\Psi_0] = E_0$. In Hartree-Fock theory[26], Ψ is assumed to be an antisymmetric product of orthogonal orbital wavefunctions $\psi_i(x)$ which depends on the coordinates of single electron.

$$\Psi_0 \approx \Psi_{HF} = \frac{1}{\sqrt{N!}}\begin{vmatrix} \psi_1(\vec{x}_1) & \psi_2(\vec{x}_1) & \dots & \psi_N(\vec{x}_1) \\ \psi_1(\vec{x}_2) & \psi_2(\vec{x}_2) & \dots & \psi_N(\vec{x}_2) \\ \vdots & \vdots & & \vdots \\ \psi_1(\vec{x}_N) & \psi_2(\vec{x}_N) & \dots & \psi_N(\vec{x}_N) \end{vmatrix}$$

Then, the expected value of total energy E_{HF} is given by

$$E_{HF} = \langle \Psi_{HF} | \hat{H} | \Psi_{HF} \rangle = \sum_{i=1}^{N} H_i + \frac{1}{2} \sum_{i,j=1}^{N} (J_{ij} - K_{ij})$$

$$H_i \equiv \int \psi_i^*(\vec{x}) \left[-\frac{1}{2} \nabla^2 - V_{ext}(\vec{x}) \right] \psi_i(\vec{x}) \, d\vec{x}$$

where H_i takes integral on the kinetic energy and electron-nucleus attraction, and

$$J_{ij} = \int \int \psi_i(\vec{x}_1) \psi_i^*(\vec{x}_1) \frac{1}{r_{12}} \psi_j^*(\vec{x}_2) \psi_j(\vec{x}_2) d\vec{x}_1 d\vec{x}_2$$

$$K_{ij} = \int \int \psi_i^*(\vec{x}_1) \psi_j(\vec{x}_1) \frac{1}{r_{12}} \psi_i(\vec{x}_2) \psi_j^*(\vec{x}_2) d\vec{x}_1 d\vec{x}_2$$

J_{ij} and K_{ij} are Coulomb integrals and exchange integrals written in terms of the orbitals. The orthonormality of orbitals leads to Hartree-Fock differential equation

$$\hat{f} \, \psi_i = \epsilon_i \, \psi_i \, , i = 1, 2, ..., N$$

$$\hat{f} = -\frac{1}{2} \nabla_i^2 - \sum_{A}^{M} \frac{Z_A}{r_{iA}} + V_{HF}(i)$$

where the first two terms in the Fock operator represent the kinetic and electron-nucleus potential energy, and the last term is the mean-field Columbic repulsion between electrons given by

$$V_{HF}(\vec{x}_1) = \sum_{j}^{N} \left(\hat{J}_j(\vec{x}_1) - \hat{K}_j(\vec{x}_1) \right)$$

$$\hat{J}_j(\vec{x}_1) = \int |\psi_j(\vec{x}_2)|^2 \frac{1}{r_{12}} \, d\vec{x}_2$$

$$\hat{K}_j(\vec{x}_1) \, \psi_i(\vec{x}_1) = \int \psi_j^*(\vec{x}_2) \frac{1}{r_{12}} \psi_i(\vec{x}_2) \, d\vec{x}_2 \, \psi_j(\vec{x}_1)$$

The Coulumb operator represents the potential experienced by an electron at position x_1 from average charge distribution of other electron in spin orbital ψ_j. The Hartree-Fock theory efficiently describes non-interacting electrons under a mean field potential. However, its neglect

of electron correlation leads to a total energy higher than the exact solution of the Schrödinger equation.

In density functional theory, electron density is being considered instead of the many-electron wavefunctions. The early Thomas-Fermi model[27] is based on uniform electron gas and formulates energy as a function of electron density only. Later, Hohenberg and Kohn[28] proved that electron density ρ(r) uniquely determines the external potential $V_{ext}(r)$ with an extra constant. Since the Hamiltonian is a function of only the external potential and the number of electrons (which can be calculated by taking integral of the electronic density), the Hamiltonian can be uniquely determined given electron density. The second Hohenberg-Kohn theorem[28] states that, similar to the variance principle, the energy obtained from any trial electron density, subject to the constraint of total number of electrons, sets an upper bound for the true ground state energy E_0, and E_0 is only achieved if and only if the input electron density is the true ground state density. These two theorems set the fundamentals of DFT in the ground state.

$$E_0 = \min_{\rho \to N} \left(F[\rho] + \int \rho(\vec{r}) V_{Ne} d\vec{r} \right)$$

$$F[\rho] = T[\rho] + J[\rho] + E_{ncl}[\rho]$$

where F[ρ] has contributions from kinetic energy T[ρ], the classical Coulomb interaction J[ρ] and non-classical electron-electron interaction $E_{ncl}[\rho]$ (e.g. self-interaction correction).

The main challenge of DFT is to find accurate expressions of T[ρ] and $E_{ncl}[\rho]$. Kohn and Sham proposed to approximate the exact kinetic energy of an interacting system using a non-

interacting reference system[29], therefore the kinetic energy and electron density are known from orbitals.

$$T_S = -\frac{1}{2}\sum_i^N \langle\psi_i|\nabla^2|\psi_i\rangle \qquad \rho_S(\vec{r}) = \sum_i^N \sum_s |\psi_i(\vec{r},s)|^2 = \rho(\vec{r})$$

Kohn and Sham accounted for the difference between T_S and the true kinetic energy T of the system by rewritting the energy functional as

$$E[\rho] = T_S[\rho] + J[\rho] + E_{XC}[\rho] + E_{Ne}[\rho]$$

where the exchange-correlation energy E_{xc} is given by

$$E_{XC}[\rho] \equiv (T[\rho] - T_S[\rho]) + (E_{ee}[\rho] - J[\rho])\,.$$

whose physical meaning is the sum of the error in using non-interacting kinetic operator and the error in classical treatment of electron-electron interaction. In order to solve E_{xc}, by using the variance principle, we can deduce the Kohn-Sham equation:

$$\left(-\frac{1}{2}\nabla^2 + \left[\int \frac{\rho(\vec{r}_2)}{r_{12}} + V_{XC}(\vec{r}_1) - \sum_A^M \frac{Z_A}{r_{1A}}\right]\right)\psi_i = \left(-\frac{1}{2}\nabla^2 + V_S(\vec{r}_1)\right)\psi_i = \epsilon_i\psi_i$$

where V_{XC}, the exchange-correlation potential, is defined as $V_{XC} = \delta E_{XC}/\delta\rho$. The Kohn-Sham equation describes a system of interacting particles using a fictitious system of non-interacting particles experiencing a local effective potential V_S, and allows us to take advantage of the power of DFT without the loss of accuracy.

The exchange-correlation potential V_{XC} still remains as an unknown term. Based on the uniform electron gas model, the local density approximation (LDA) is the most fundamental way to address the exchange-correlation potential. Under its assumption, the exchange-correlation energy E_{XC} can be written in the form

$$E_{XC}^{LDA}[\rho] = \int \rho(\vec{r})\epsilon_{XC}(\rho(\vec{r}))\ d\vec{r}$$

where $\varepsilon_{XC}(\rho(r))$ is the exchange-correlation energy per particle of uniform electron gas of density $\rho(r)$, and $\rho(r)$ represents the possibility that there is an electron at a position. ε_{XC} can further be split into exchange and correlation terms

$$\epsilon_{XC}(\rho(\vec{r})) = \epsilon_X(\rho(\vec{r})) + \epsilon_C(\rho(\vec{r})).$$

and the exchange part is given by the Dirac form

$$\epsilon_X = -\frac{3}{4}\left(\frac{3\rho(\vec{r})}{\pi}\right)^{1/3}$$

The functional form of correlation energy density ε_C, is unknown and has been studied using quantum Monte Carlo methods[30]. Since in general the exchange energy is underestimated while correlation energy is overestimated, cancellation of errors may occur. LDA has been report to predict accurate bond lengths of molecules[31] but less satisfactory in the calculation of energies[32], especially in systems with heavy electron-electron interactions.

Gradient expansion approximation (GEA) methods improves LDA by also considering the first order gradient of charge density $\nabla\rho(r)$ to account for the non-homogenity of true electron density, which has the expression

$$E_{XC}^{GEA}[\rho_\alpha, \rho_\beta] = \int f(\rho_\alpha, \rho_\beta, \nabla\rho_\alpha, \nabla\rho_\beta)\ d\vec{r}$$

In generalized gradient approximation (GGA), the energy functional depends on both the density and its gradient. It is reported to significantly improve the descriptions of binding energies of molecules compared to LDA[33].

Classical molecular dynamics

Molecular dynamics[23], [34] calculate the time-dependent behavior of a system and is widely used to investigate the structure, dynamics and thermodynamics in materials science[35] and biophysical applications[36]. Classical MD simulations use empirical force fields to describe the interactions of collections of atoms in the form of potential $U(r_1, \ldots, r_N)$ as a function of their positions r_i. Each atom i at position r_i is treated as a point with mass m_i and fixed charge q_i. The force acting on i^{th} atom is determined by

$$\mathbf{F}_i = -\nabla_{\mathbf{r}_i} U(\mathbf{r}_1, \cdots, \mathbf{r}_N) = -\left(\frac{\partial U}{\partial x_i}, \frac{\partial U}{\partial y_i}, \frac{\partial U}{\partial z_i}\right)$$

According to Newton's equation of motion, the time evolution of a set of interacting particles is

$$\mathbf{F}_i = m_i \frac{\mathrm{d}^2 \mathbf{r}_i(t)}{\mathrm{d}t^2}$$

The set of N second-order differential equations is solved numerically at discrete time steps to determine the trajectory of an atom. At each step, the force acting on each atom is computed using the force field and the position and velocity of each atom is updated accordingly. Numerous numerical algorithms have been developed for integrating the equation of motion, including the Verlet and Leap-frog algorithm. The Verlet algorithm uses the positions and accelerations and does not rely on explicit velocities. By Taylor expansion,

$$r(t + \delta t) = r(t) + v(t)\delta t + \frac{1}{2} a(t)\delta t^2$$

$$r(t - \delta t) = r(t) - v(t)\delta t + \frac{1}{2} a(t)\delta t^2$$

Adding these two equations gives

$$r(t + \delta t) = 2r(t) - r(t - \delta t) + a(t)\delta t^2$$

On the other hand, the Leap-frog algorithm firstly calculates the velocities at time t + dt/2 and uses it for the positions at t + dt:

$$v\left(t+\frac{1}{2}\delta t\right)=v\left(t-\frac{1}{2}\delta t\right)+a(t)\delta t$$

$$r(t+\delta t)=r(t)+v(t+\frac{1}{2}\delta t)\delta t$$

The choice of a proper time step is limited by the highest frequency vibration. Usually the time step should be at least one order of magnitude lower than the fastest time scale in the system. For example, in case the C-H bond stretching (10^{-14} s) is the fastest mode, the limit of time step should be 1 fs. A time step that is too large can potentially cause undesired atoms collision and system explosion.

Current force fields provide a good compromise between accuracy and computational cost. They are usually derived from first principles modeling of small molecules (e.g. initial guess of partial charge based on electronic densities) or fitted according to experimental results (e.g. structural information from X-ray crystallography and NMR, neutron scattering and thermodynamic data), and the results of simulation would only be accurate if the force field represents the real interaction of atoms. The basic formulation of force field includes bonded terms for covalent interactions and non-bonded terms for long-range electrostatics and van der Waals interactions:

$$E_{total} = E_{bonded} + E_{non\text{-}bonded} = (E_{bond} + E_{angle} + E_{dihedral}) + (E_{electrostatic} + E_{vdW})$$

AMBER[37], CHARMM[38] and OPLS[39] force fields are commonly used for large molecules such as proteins and polymers in condensed phases. For example, the energy terms described in CHARMM force field look like

$$
\begin{aligned}
U(\vec{R}) \;=\; & \underbrace{\sum_{bonds} k_i^{bond}(r_i - r_0)^2}_{U_{bond}} + \underbrace{\sum_{angles} k_i^{angle}(\theta_i - \theta_0)^2}_{U_{angle}} + \\
& \underbrace{\sum_{dihedrals} k_i^{dihe}[1 + \cos(n_i\phi_i + \delta_i)]}_{U_{dihedral}} + \\
& \underbrace{\sum_i \sum_{j \neq i} 4\epsilon_{ij}\left[\left(\frac{\sigma_{ij}}{r_{ij}}\right)^{12} - \left(\frac{\sigma_{ij}}{r_{ij}}\right)^{6}\right] + \sum_i \sum_{j \neq i} \frac{q_i q_j}{\epsilon r_{ij}}}_{U_{nonbond}}
\end{aligned}
$$

Some force fields also take into account polarizability effects where a particle's effective charge is influenced by the electrostatic interactions with the neighbors. The Drude oscillator model includes a positively-charged core particle and a negatively-charged particle attached to the core particle through a harmonic oscillator potential. Some examples of polarizable force field for water includes SWM4-DP[40] and BK3[41] and they are reported to show reasonably good consistency with diffraction experiment results[42].

The computation of non-bonded interactions to interatomic forces is time-consuming since it requires a large number of pairwise computations. To address this problem, a neighbor list is defined such that the force calculation of atoms with distances r_{ij} farther than the potential cutoff r_{cut} plus a "skin" distance is skipped (Fig. 2.1). Over the next few steps, only the pairs in the neighbor list are checked. The neighbor list must be reconstructed before the particles outside the range (black) penetrate the potential cutoff sphere.

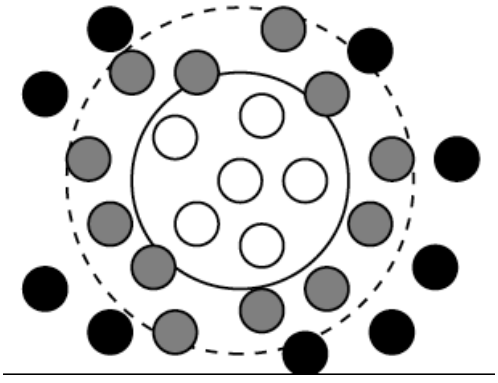

Fig. 2.1 Construction of a neighbor list. The potential cutoff range is shown in solid black circle and the list range is within dashed line.

The current limitations of MD include the reliability of force field, its inability to model quantum effects as well as time/size limitations. It is computationally expensive to model conformational changes that happen over large time scales (e.g. protein folding may take a few minutes). Many advanced algorithms have been developed to study slow conformational changes and activated process.

Chapter 3

Development of a QM/MM model for free energy calculations of nanoscale adsorption

3.1 Introduction

Free energy profile[43] is essential in understanding the reaction pathways and mechanisms in chemical reaction and physical processes. Accurately determining the free energy profile along the reaction coordinate (i.e. potential of mean force) requires the use of enhanced sampling methods, such as umbrella sampling[44] and metadynamics[45], to overcome local energy minima and sample the transition states. Umbrella sampling breaks reaction coordinates into several windows and applies a series of harmonic potentials to restrain the reaction coordinate close to the center of each window. The potential of mean force (PMF) can be recovered by performing weighted histogram analysis method[46] (WHAM) or multistate Bennett acceptance ratio[47], [48] (MBAR) method to remove the biasing of restraints from the sampling of reaction coordinate values.

However, the computation of free energy profile at *ab initio* level in large systems is not feasible due to poor scaling with system size, while the accuracy of semi-empirical or classical methods is often unsatisfactory. In this study, we aim to develop a quantum mechanical/molecular mechanical (QM/MM) model of ion adsorption to graphene to perform

energy corrections to a classical PMF. One computationally-efficient method of such correction is the weighted thermodynamic perturbation (wTP) method[49], which includes three main steps:

(1) Umbrella sampling using low-level Hamiltonian;

(2) Generate low-level free energy profile using the MBAR analysis;

(3) Calculate free energy difference between high- and low-level Hamiltonian based on the sampled configurations and their weight factors generated from MBAR.

Specifically, the weight of the l^{th} configuration in the i^{th} biased simulation under the low-level Hamiltonian U_L is[49]

$$w_L(\mathbf{x}_{i,l}) = \frac{e^{-\beta\left[U_L(\mathbf{x}_{i,l})-f_L\right]}}{\sum_{k=1}^{S} N_k e^{-\beta\left[U_k^{(b)}(\mathbf{x}_{i,l})-f_k^{(b)}\right]}} = \frac{e^{\beta f_L}}{\sum_{k=1}^{S} N_k e^{-\beta\left[W_k(\mathbf{x}_{i,l})-f_k^{(b)}\right]}},$$

where $x_{i,l}$ represents the l^{th} frame among N_i configurations in the i^{th} biased simulation, and W is the restraining bias. For a certain histogram bin, the free energy difference between the high- and low-level Hamiltonian can be obtained by[49]

$$\Delta F(\eta) = -\frac{1}{\beta}\ln\frac{\sum_{i=1}^{S}\sum_{l=1}^{N_i} w_L(\mathbf{x}_\eta)\,\delta\left(\eta_{(i,l)}-\eta\right)e^{-\beta[U_H(\mathbf{x}_\eta)-U_L(\mathbf{x}_\eta)]}}{\sum_{i=1}^{S}\sum_{l=1}^{N_i} w_L(\mathbf{x}_\eta)\,\delta\left(\eta_{(i,l)}-\eta\right)} = -\frac{1}{\beta}\ln\frac{\sum_{i=1}^{S}\sum_{l=1}^{N_i} w_L\left(\mathbf{x}_{\eta_{(i,l)}}\right)e^{-\beta\left[U_H\left(\mathbf{x}_{\eta_{(i,l)}}\right)-U_L\left(\mathbf{x}_{\eta_{(i,l)}}\right)\right]}}{\sum_{i=1}^{S}\sum_{l=1}^{N_i} w_L\left(\mathbf{x}_{\eta_{(i,l)}}\right)},$$

where the subscripts H and L denote the high- and low-level Hamiltonians, $\eta_{(i,l)}$ is the histogram bin that the l^{th} configuration in the i^{th} baised simulation belongs to, and $w_L(x_\eta)$ is the unbiased weight of the sample in the bin η under the low-level Hamiltonian.

3.2 Computational methods

The low-level calculations that we would like to perform energy corrections on is classical MD simulations carried out using the LAMMPS[34] software package. Initial configurations, built using fftool and Packmol[50], consist a selected anion (F^-, Cl^-, $NO3^-$, SCN^-), a graphene flake of 180 atoms, and 700 water molecules above graphene in a unit box of 22 Å x 22 Å x 150 Å. Rectangular prism periodic boundary condition was applied and the dimension in the *z* direction was kept large to prevent interaction of periodic images. Lennard-Jones type force field parameters for anion-graphene interactions have been developed by Misra *et al* from symmetry-adapted perturbation theory (SAPT)[51]. The classical Drude oscillator model[52] with Thole damping has been used for carbon to account for the polarization of graphene from the electric field exerted by water and anion. In the model, the Drude Particle (DP, m_D = 0.4 g mol^{-1}) and Drude Core (DC, m_C = 11.61 g mol^{-1}) of carbon possess point charges and the DP is attached to DC via harmonic spring. DPs are maintained at significantly lower temperature of 1K whereas DCs are kept at 300K by two separate Nosé-Hoover thermostats[53] with time constants 5 fs and 0.1 ps, respectively. SHAKE algorithm[54] was employed for rigid SPC/E water[55] and the time step was 1.0 fs. Umbrella sampling was performed by fixing the anion at a distance varying from 10 Å to 2 Å away from the graphene surface, with window size of 1 Å and force constant of 4 kcal/mol/$Å^2$. For each distance, an individual trajectory was deposited, containing 800 ps canonical NVT dynamics with frames stored every 100 fs.

Two snapshots from the MD trajectory, where an anion is 10 and 2 Å apart from graphene surface, are chosen as the starting models for QM/MM model development. The QM region is selected to be a water sphere of certain radius r around the anion, plus the finite graphene flake

of around 180 atoms with edges terminated by hydrogen. The remaining system consists water molecules only and is treated with classical MM.

Table 3.2.1. QM radius size and number of QM atoms in the model. Configs 1 and 2 refer to configurations where the anion is 10 and 2 Å away from graphene surface.

Radius(Å)	**4**	**5**	**6**	**7**	**8**	**9**	**10**
Config 1	245	272	305	362	431	512	617
Config 2	269	290	317	347	392	440	515

In QM/MM single point calculations, TeraChem[56] and Amber 14[57] were used for the QM and MM regions, respectively. The QM/MM total energy is expressed by:

$$E_{QM/MM} = E_{QM} + E_{QM-MM} + E_{MM}$$

where in our case, E_{QM-MM} is zero since the QM and MM regions only consist whole water molecules and no covalent bond crosses from QM to MM border. The QM region is modeled with DFT using the range-separated exchange-correlation functional ωPBEh[58] with 6-31g* basis set, and the MM region is treated with TIP3P water force field[59]. In order to mimic the periodic boundary condition from polarizable force field trajectories, cylindrical TIP3P water charge field was built by creating replicas of unit box around itself followed by radial truncation. Initial radius of truncation is defined to be half the length of graphene diagonal, while radius increment dr ranges from 0 to 12 Å, resulting in around 1200~8400 additional point charges. The rigid binding energy of anion, as defined by $E_{binding}$ = E(with anion) – E(without anion) – E(anion), is used as a metric to determine the convergence of QM region size.

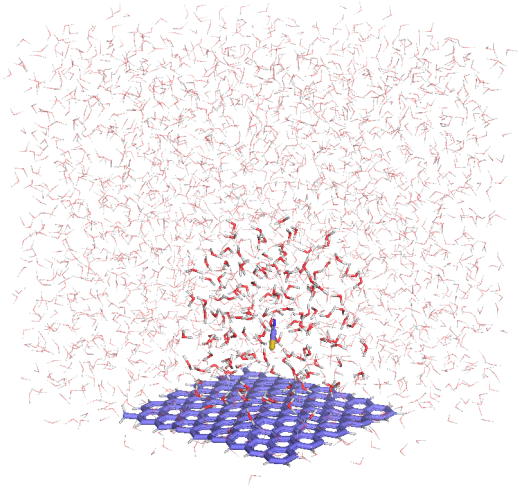

Fig 3.2.1 QM/MM single point calculations setup for PMF correction of ion adsorption to graphene. The QM region is highlighted in bold surrounded by MM point charges of water.

3.3 Results and discussion

The anion-graphene interaction was parametrized based on binding energies of anion to large polycyclic aromatic hydrocarbons such as coronene and circumcoronene using sSAPT0, which decomposes binding energies into electrostatics, exchange, dispersion and induction components[60]. Firstly, we tested the influence of first principle methods on the binding energy of thiocyanate ion to circumcoronene by comparing sSAPT0/jun-cc-pvdz results with range-separated exchange-correlation functional ωPBEh with 6-31g* basis. Three anion orientations: S-Facing, N-Facing and tangential configurations were considered. From Fig. 3.3.1, the SAPT binding energies agree well with ωPBEh results, except that it tends to overestimate the binding energy of tangential configuration at short anion-graphene distances < 2.5 Å. It has been reported that SAPT0/jun-cc-pvdz is remarkably accurate compared to higher levels of methods, since most of its accuracy comes from error cancellation between the uncoupled treatment of dispersion in SAPT0 and the limited ability of the basis set to represent electron correlation.

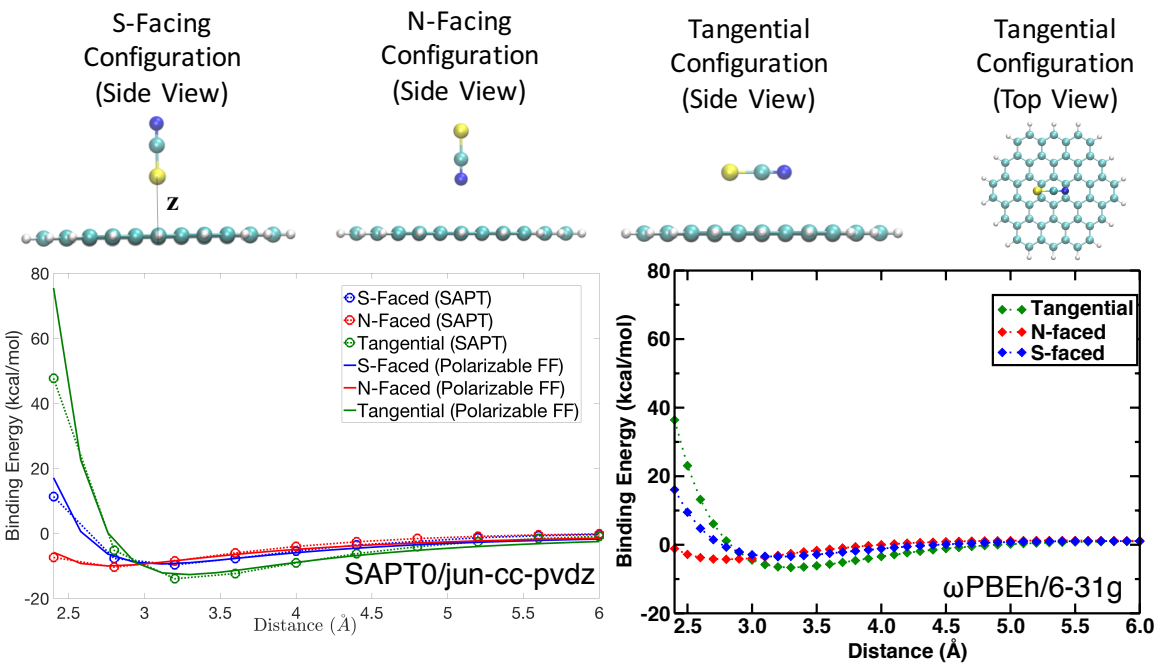

Fig. 3.3.1 Comparison of thiocyante binding energies to circumcoronene between sSAPT0/jun-cc-pvdz and ωPBEh/6-31g*

Classical PMF of ion adsorption to graphene has been computed with umbrella sampling and the Weighted Histogram Analysis Method (WHAM), as shown in Fig 3.3.2. It reveals that kosmotropic ions (e.g. F^-) are repelled from water-graphene interface, whereas there exists an equilibrium position for chaotropic ions (e.g. SCN^-).

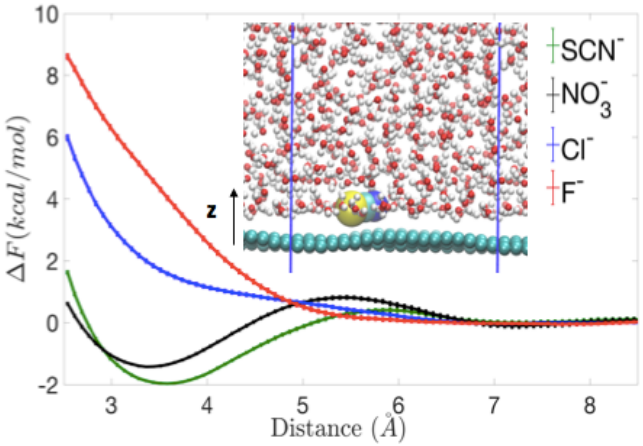

Fig. 3.3.2 Classical ion adsorption PMF from polarizable force field molecular dynamics (Courtesy of Misra *et al*.)

The similarity between the Hamiltonians of neighboring windows in umbrella samplings is critical to the statistical reliability. To this end, Klimovich *et al.* has proposed an overlap matrix to quantify the magnitude of phase-space overlap[61], which is a K x K matrix with entries:

$$O_{ij}=\sum_{n=1}^{N}\frac{N_i e^{\beta G_i-\beta U_i(x_n)}}{\sum_{k=1}^{K}N_k e^{\beta G_k-\beta U_k(x_n)}}\frac{e^{\beta G_j-\beta U_j(x_n)}}{\sum_{l=1}^{L}N_l e^{\beta G_l-\beta U_l(x_n)}}$$
$$=\sum_{n=1}^{N}\frac{N_i p_i(x_n)}{\sum_{k=1}^{K}N_k p_k(x_n)}\frac{p_j(x_n)}{\sum_{l=1}^{L}N_l p_l(x_n)}$$

The term $\exp(\beta G_i-\beta U_i)$ represents the probability $p_i(x_n)$ of sample x_n to occur when simulating state i, and the N samples are collected with N_1 samples from $p_1(x)$ distribution, N_2 samples from $p_2(x)$, etc. A strong biasing potential may limit the samples within a small region around the center of the biasing potential, whereas a weak biasing potential may not guarantee sufficient sampling around the center of the window. An overlap between neighboring windows larger than 0.03 seems to be empirically sufficient to yield a reliable free energy estimate. We tested two cases, one with the original window size of 1 Å and another with smaller window of 0.5 Å in umbrella sampling, and the resultant first off-diagonal elements of matrices are shown in Fig 3.3.3. It seems a window size of 1 Å already has sufficient phase-space overlap for subsequent analysis.

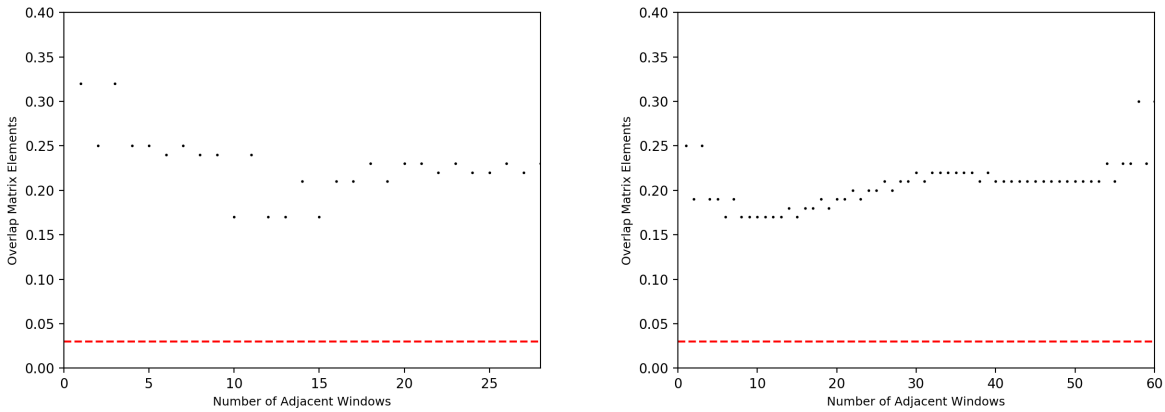

Fig. 3.3.3 The magnitude of overlap matrix elements for the neighboring windows for window size of 1 Å (left) and 0.5 Å (right). The red lines represent a threshold of 0.03.

QM/MM single point energies, which requires the accurate determination of a reasonable QM region/size, are the key components for PMF correction. We started QM/MM model construction by firstly choosing the QM radius to be 10 Å around fluoride, which is the largest value possible inside the original unit box to isolate the influence of external charge field only. The resultant binding energies with different radii of charge field is shown in Fig. 3.3.4, in which the dashed line represents a box without external charge field. It is observed that dr < 4 Å has little effect on ion binding energy, whereas the binding energies with dr = 6, 8, 10 Å converge around -192 kcal/mol.

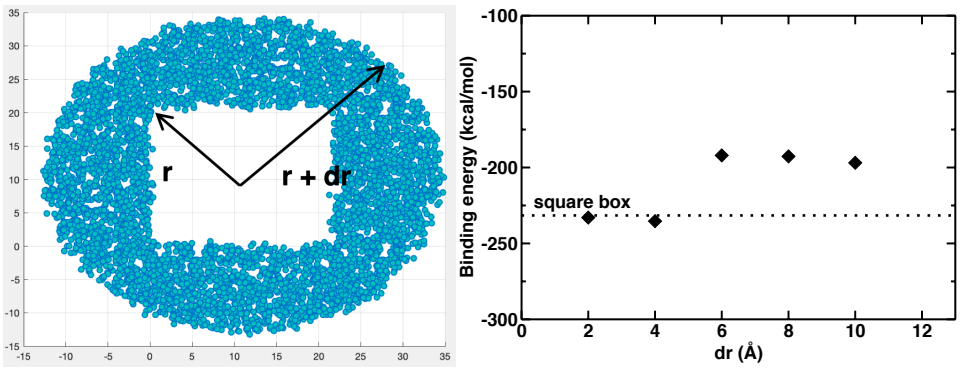

Fig. 3.3.4 (left) Projection of outside water charge field on x-y plane. Each blue dot represents a single point charge. (right) Calculated binding energies of fluoride with different radii of water charge field around the unit box. The QM radius is set to be 10 Å.

As the binding energy of fluoride is assumed to converge with dr = 8 Å external charge field, a two-point test was adapted to estimate the smallest QM region size, rather than sticking with largest possible sphere. Based on aforementioned two configurations, when the fluoride-graphene distance is 10 and 2 Å respectively, we calculate the binding energy of fluoride with dr = 8 Å cylindrical water charge field, as shown in Fig 3.3.5. When fluoride is far away from graphene (config 1), the binding energy roughly converges when QM radii is larger than ~7Å, whereas when fluoride is in vicinity of graphene surface around the edge of the water box (config 2), the QM size seems to have limited effect on the binding energy due to incomplete solvation shell.

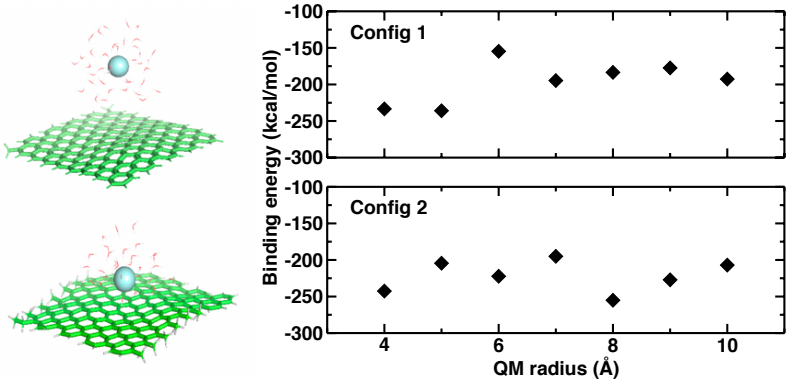

Fig 3.3.5 (left) A snapshot of QM regions in which the fluoride-graphene distance is 10 and 2 Å, respectively. (right) Binding energy of fluoride ion with respect to different QM radii in two configurations, each with applied charge field dr = 8 Å.

We also tested the convergence of the size of the cylindrical TIP3P water charge field for water-graphene-SCN^- system, using the same approach for F^-. We noticed that the water molecules at the top of the box in original classical MD trajectories are not evenly distributed. To solve this issue, we have truncated the box above z = 90 Å, and a comparison of the rigid binding energies of SCN^- with different radii of water charge field around the box is shown in Fig 3.3.6, when the thiocyanate-graphene distance is 10 and 2 Å, respectively. The QM radius is 10 Å and consists a water sphere around the anion plus graphene. The overall difference of original and truncated box doesn't seem to be very significant. The variation of binding energies is much smaller compared to F^-, and the energy start to converge around dr = 9-10 Å, slight larger than what is needed for F^-.

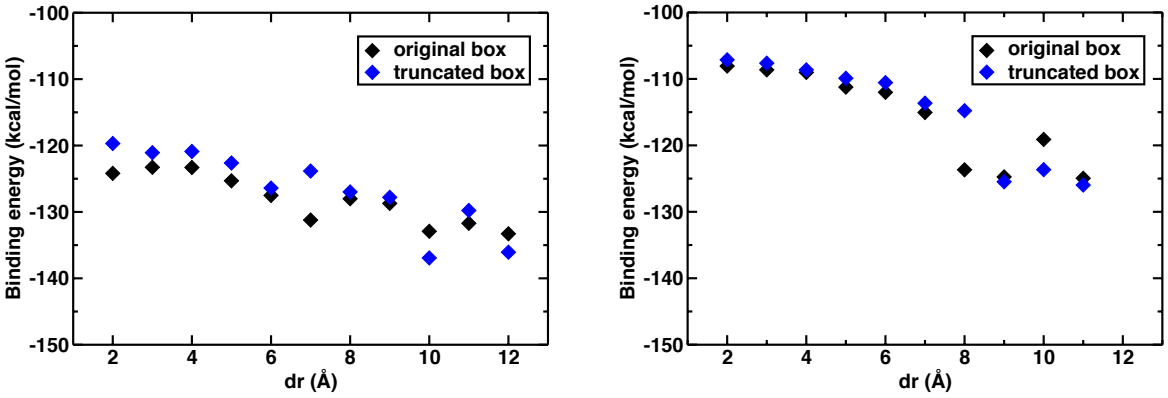

Fig. 3.3.6 Calculated binding energies of SCN^- with different radii of water charge field around simulation box. The thiocyanate-graphene distance is 10 Å (left) and 2 Å (right).

3.4 Conclusion

A nanoscale QM/MM model for the PMF correction of ion adsorption to graphene was constructed based on classical MD trajectories. It improves the existing modeling by taking into account many-body polarizations and long-range electrostatic interactions, and sets a basis for a

more accurate description of free energy changes in nanofluidic transport. Future work should involve calculating more frames of QM/MM single point energies based on classical MD snapshots, using the weighted thermodynamic perturbation theory to perform energy correction to the classical PMF, and smoothing the obtained curve to reduce statistical noise.

Chapter 4

Ab initio molecular dynamics study of coronene and defects

4.1 Introduction

Water exhibits unique properties under confinement that are distinct from properties of bulk water. Atomistic modeling can provide valuable insight into differences in nano-confined (e.g., by nm-scale carbon nanotubes) water and salt solutions. However, accurate, first-principles modeling of molecular interactions is necessary to predict emergent properties. To better understand the graphene-water interface in such systems, we performed *ab initio* molecular dynamics on representative confined systems. We investigate the nanoscale solvation behavior of selected ions on coronene and circumcoronenes as finite graphene models. We investigate the degree of charge transfer between the ion and water with range-separated hybrid density functional theory as well as how that charge transfer fluctuates during dynamics. We also investigate how defects alter these dynamics and solvation in model systems.

4.2 Computational methods

The initial configurations were prepared with the Packmol[50] package by randomly placing a selected anion (SCN^-, NO_3^-, Cl^-, F^-) and water molecules in the upper sphere above coronene ($C_{24}H_{12}$) surface while ensuring the density of water to be ~1g/mL. In order to examine the effect of system size, two larger systems circumcoronene ($C_{54}H_{18}$), and circumcircumcoronene

($C_{96}H_{24}$) were set up with the same approach. These three models include 7, 20 and 60 water molecules, respectively. Fig. 4.2.1 shows a graphical representation of the initial geometry of a circumcoronene-water-nitrate ion system.

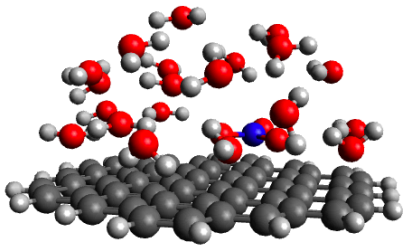

Fig 4.2.1 Snapshot of a sample circumcoronene-water-nitrate ion model

Ab initio molecular dynamics (AIMD) simulations were performed on different sizes of the coronene-water-ion system using the TeraChem[56] GPU-accelerated quantum chemistry package for charge-transfer analysis. The calculations were carried out using either the B3LYP[62] meta-generalized-gradient approximation (GGA) hybrid exchange-correlation (xc) functional, or the long-range corrected, hybrid GGA xc functional ωPBEh[58]. The performance of 6-31g* and 6-31g basis sets, as well as the Grimme's D3 dispersion correction[63], were evaluated in benchmarking. Time step was set to 0.5 fs and the temperature was held at 300 K with the Langevin thermostat[64]. Throughout dynamics of 50 ps, spherical boundary condition is applied throughout dynamics to constrain water molecules within the upper sphere, enforced by

$$U_{constr}(r) = k((r-R_{center})-R)^2$$

where individual R values depends on the system size, and the force constant k was set to be 10 kcal/(mol $Å^2$).

4.3 Results and discussion

The Mulliken charge fluctuation of anions in coronene-water-anion system has been analyzed. Firstly, the effect of system size was estimated by comparing the Mulliken charge of fluoride ion in three sized systems (Fig 4.3.1). It has been observed that the distribution of partial charge in the coronene system has substantial deviation from the larger ones probably due to incomplete solvation and the edge effect, whereas circumcoronene and circumcircumcoronene-based systems showed closer similarity. We therefore conclude the smallest coronene system is insufficient for a proper analysis of charge transfer.

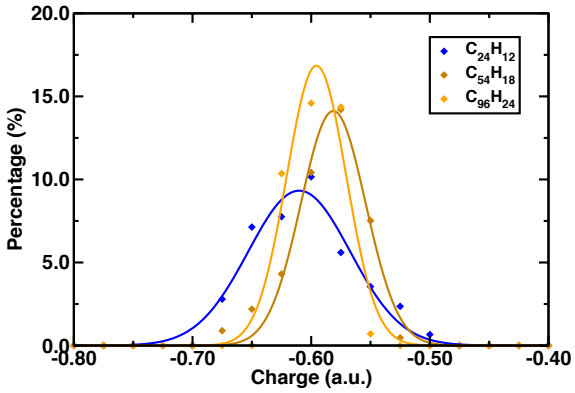

Fig 4.3.1 Histogram of fluoride Mulliken charge in three systems with different sizes

Selecting circumcoronene-water-anion system as our model, we benchmarked different combinations of functionals and basis sets and examined their effect on anion partial charge: (1) ωPBEh/6-31g (2) ωPBEh/6-31g* (3) B3LYP/6-31g* (4) ωPBEh/6-31g* with D3 dispersion correction (Fig. 4.3.2). Regardless of our choice of functionals or basis sets, the partial charge distribution of fluoride was centered around -0.6, which is unreasonably low compared to other anions.

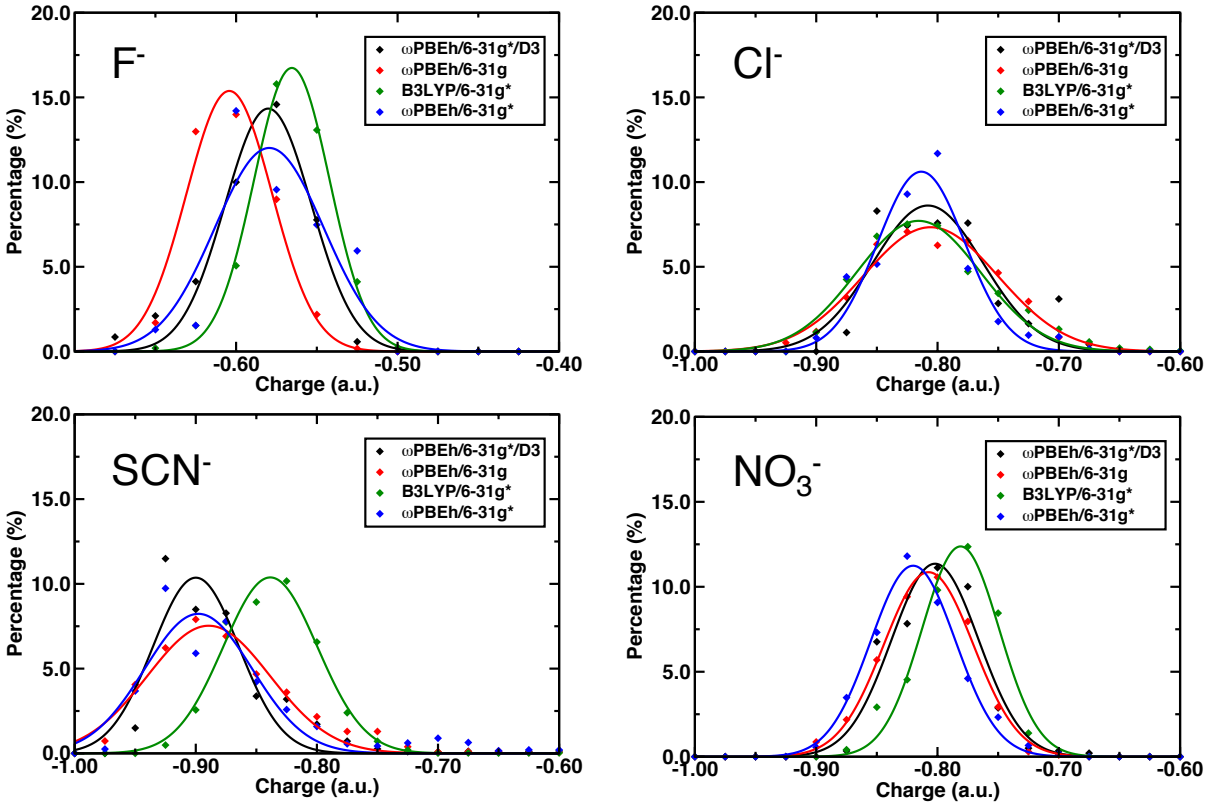

Fig. 4.3.2 Histograms of the Mulliken charge of anions (SCN^-, NO_3^-, Cl^-, F^-) in circumcoronene-water-anion systems using different functionals and basis sets.

Structural analysis was performed to elucidate the charge transfer anomaly during solvation. The radial distribution function of O-F^- and O-Cl^- pair were plotted with VMD[65] from an ωPBEh/6-31g trajectory of 5 ps (Fig 4.3.3), from which the cutoffs for their 1st coordination shells have been determined. The average charge of water molecules in fluoride's 1st coordination shell is shown to be remarkably lower than those of chloride (Fig 4.3.4). Also, a fraction of F^- negative charges seemed to have been distributed to circumcoronene, which does not appear physically meaningful. In general, fluoride seems to induce stronger localized charge transfer between anion and water. To evaluate the accuracy of DFT functionals, we ran higher-level DLPNO-CCSD(T)/aug-cc-pvdz single point calculations in Orca[66] for random snapshots

of fluoride-water clusters, from which their Mulliken charge is reported to be around -0.94 on average. The coupled-cluster calculation result demonstrates that our DFT functionals fail to correctly describe the electronic structure of fluoride in water.

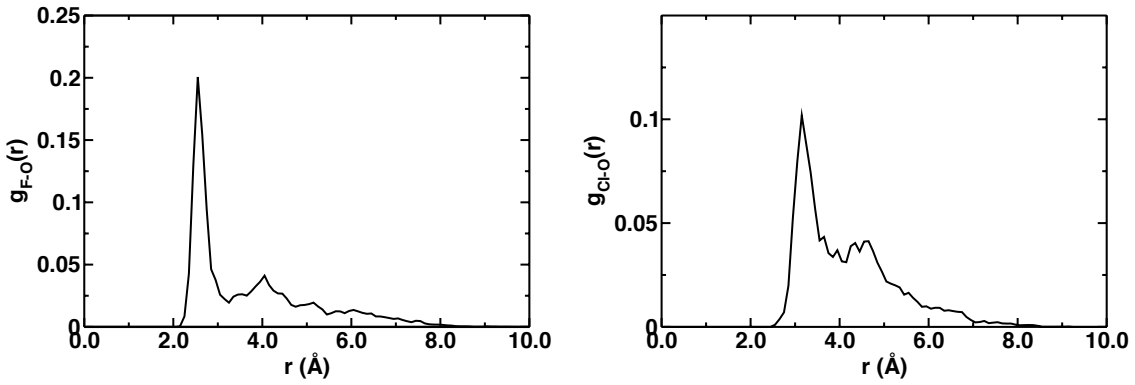

Fig 4.3.3 Radial distribution functions for O-F^- and O-Cl^- pairs in fluoride/chloride-water-circumcoronene system

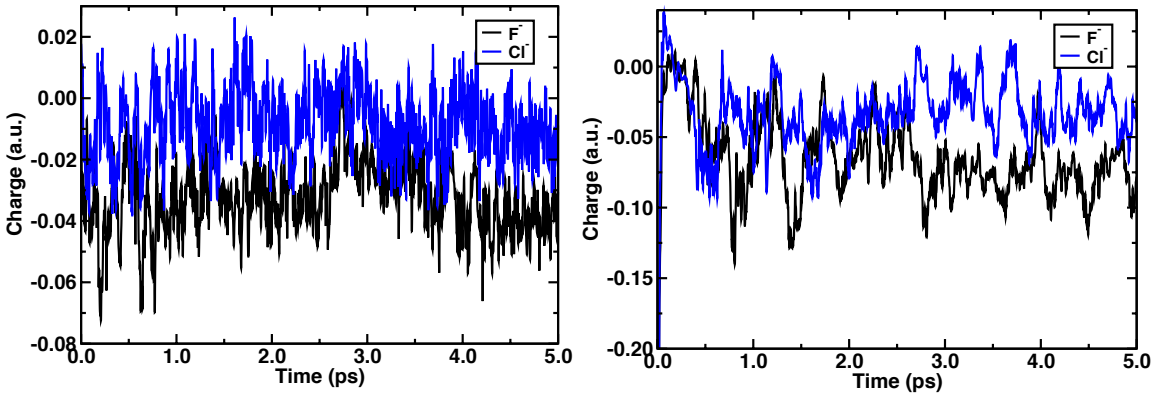

Fig 4.3.4 Average charges of (left) water in the 1st coordination shell, and (right) circumcoronene in fluoride/chloride-water-circumcoronene system

Further effort has been devoted to tuning the DFT functional ωPBEh, attempting to reliably reproduce fluoride partial charge. The range-separated hybrid functional ωPBEh combines 80% PBE GGA exchange and 20% HF exchange at short range with asymptotically correct HF

exchange for the long range[67]. The percentage of Hartree-Fock exchange (HFX) and the range separation parameter ω were altered to observe the effect of exact exchange and the effect of long-range exchange, respectively. HFX was tuned from as low as 10% to 50% with an increment of 10%, whereas the range separation parameter ω was altered from 0.001 $bohr^{-1}$ to 0.4 $bohr^{-1}$ with increments of 0.1 $bohr^{-1}$. The simulations were carried out with basis set 6-31g* and D3 dispersion correction. As shown in Fig. 4.3.5, for a fixed percentage of Hartree-Fock exchange, increasing ω tunes the partial charge to be more negative. Similarly, for a fixed range separation parameter ω, increasing HFX also result in a more negative value. However, within the range of values we tested, at HFX = 50% and ω = 0.4 $bohr^{-1}$, the most negative partial charge achievable is around -0.68, which is still far from the targeted value.

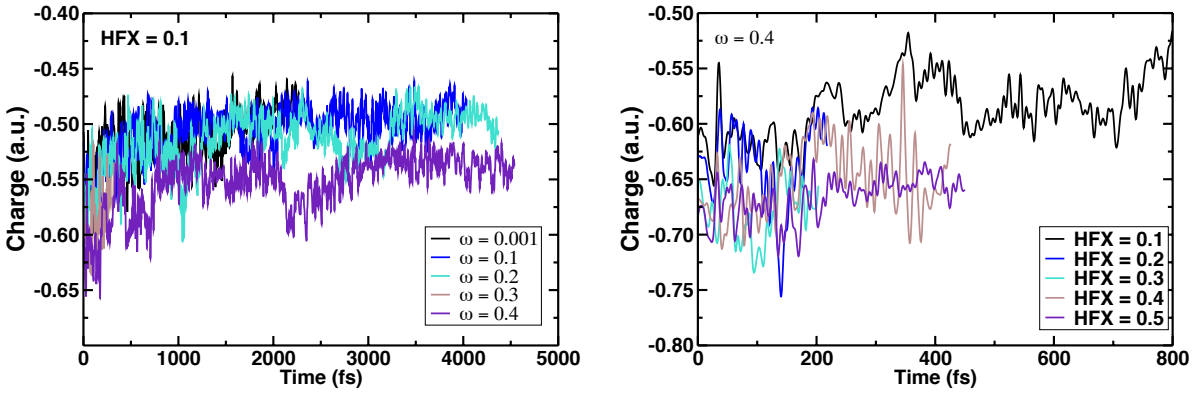

Fig 4.3.5 Charge fluctuation of fluoride ion (left) while altering ω from 0.001 to 0.4 $bohr^{-1}$ and keeping HFX fixed at 10%, and (right) altering HFX from 10% to 50% and fixing ω from 0.4 $bohr^{-1}$.

How topological defects on coronene may influence the solvation process is also an open question of our primary interest. We started by introducing various vacancies on circumcoronene involving mostly five and seven-membered rings (e.g. Stone-Wales defect and double vacancy[68]) and analyzing the partial charges with a similar approach. The charges of carbon

atoms of vacancy region (in red and green) was compared to that of defect-free circumcoronene. Results shown in Fig. 4.3.6 suggest that the carbons that form defects are predominantly neutral, and anion charge in water does not seem to be affected by the vacancy. It is worth noting that those defects are associated with large formation energy (~ 4.8 – 10.4 eV[68])and are rarely observed in experiments alone, thus for the next step we moved beyond simplest models and consider more realistic and complex defects, e.g. those involving hydroxyl groups.

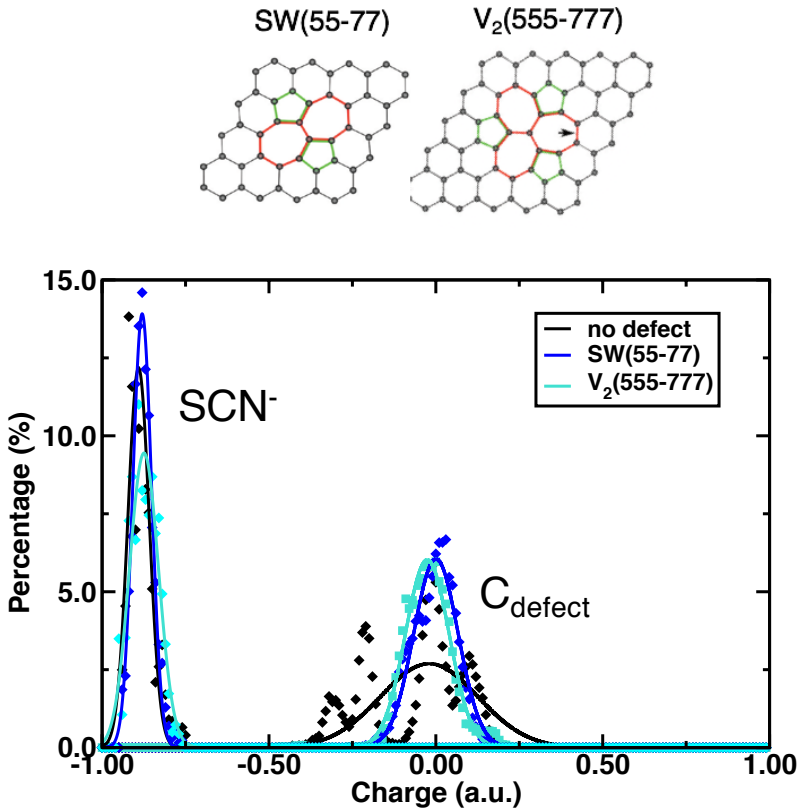

Fig 4.3.6 Comparison of partial charges of carbons on defect and thiocyanate ion between circumcoronene which is defect-free, with Stone-Wales defect, and with double vacancy 555-777.

Topological defects on graphene are known to be the center of chemical activities[69], as they influence the adsorption and reactivity of functional groups at graphene surface. Stone-

Wales defects, for example, are able to stabilize the adsorbed hydroxyl groups with stronger binding as well as raising the energy barrier for recombination and water formation compared to pristine graphene[70]. Here we chose a model of hydroxyl pairs adsorbed on a Stone-Wales defect followed by water formation[70], during which an epoxy group is left on the defect. We studied the charge transfer between the resultant structure and selected cations (Li^+, Na^+) in water (Fig 4.3.7). AIMD reveals a large difference between lithium and sodium Mulliken charge, whereas the partial charges of the epoxy oxygen remained similar despite the discrepancy in ion-oxygen distance along the trajectory. This finding suggests that major charge transfer of solvated cation near an epoxy group happens within the solvation shells, instead of between cation and epoxy group.

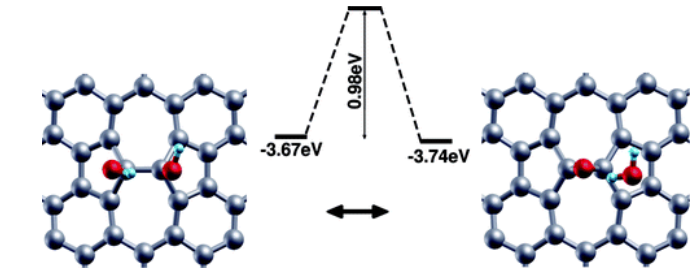

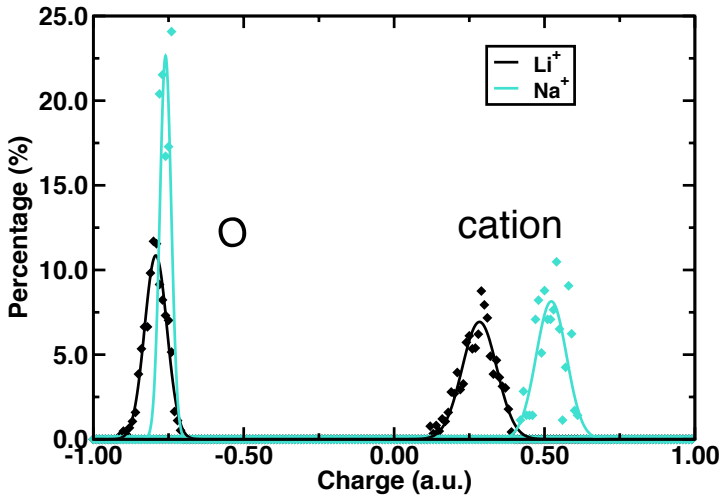

Fig 4.3.7 Comparison of partial charges of oxygen, and lithium/sodium cations after water formation in hydroxyl groups aggregation on a Stone-Wales defect (Adapted from Ref[70]).

4.4 Conclusion

In this study, we used *ab initio* molecular dynamics (AIMD) to study the nanoscale solvation behavior by constructing finite ion-water-coronene models. Benchmarking and tuning range-separated hybrid functional ωPBEh informed the limitation in the accuracy of DFT methods to predict the electronic structure of solvated halide (F^-) in water clusters. The simulations revealed how intrinsic charge transfer and molecular interactions dictate the solvation process, as well as the the impact of vacancy defects and polar functional groups on solvated cations/anions. Future direction could involve comparing different charge schemes (e.g. Voronoi deformation density charge, Hirshfeld charge), introducing more diverse and more complex geometries of functional groups to study the surface preference of ions, as well as adapting periodic boundary conditions to overcome the limitations of finite models.

Chapter 5

Molecular simulation study of dielectric-induced ionization behavior in nanoporous polyamide membranes

5.1 Introduction

Water scarcity is one of the largest global challenges, affecting two-thirds of the world population. The advancement of membrane materials for water purification processes such as desalination is in great demand to produce clean water from contaminated sources or the sea. Polyamide selective layers, formed through the interfacial polymerization of a diamine with a tri-acid chloride, has emerged as the gold standard for reverse osmosis and nanofiltration applications[71], [72]. However, the advancement of membrane technologies is hindered by our limited understanding of their structure-property-performance relationships. The membrane's charge density (carboxyl groups formed from the hydrolysis of residual acid chlorides and unreacted amines) following their ionization influences interactions between the membrane surface and charged constituents in the feed water, and thus has a great impact on the performance of membranes[73]. In this study, we adapted molecular dynamics simulations and density functional theory to validate the dielectric-driven mechanism of location-dependent anomalous ionization behavior of carboxyl group in polyamide membranes, which highlights the role of nanoconfinement in membrane operation and provides fundamental understanding for future membrane design principles.

5.2 Computational methods

Classical molecular dynamics (MD) simulations were performed to calculate the dielectric constant of bulk and confined water using the LAMMPS[34] (7 Aug 2019) package. To ensure insensitivity to the water model, results were compared using the rigid SPC/E[55], TIP4P/ε[74], and flexible SPC/Fw[75] water models. The dielectric constant of bulk water was obtained using a box of 1,000 water molecules that was simulated with rectangular prism periodic boundary conditions. The dielectric constant of confined water was estimated using a model of 1,047 water molecules in a 2 nm diameter cylinder. This structure was generated using Packmol[50] by randomly placing the water molecules in the cylinder of diameter 2 nm and length 10 nm with a density of 1.0 g cm^{-3}. The dimension of unit box was then expanded to 110Å x 110Å x 110Å to avoid undesired interactions between cylinders in the radial direction. Both structures were equilibrated for 100 ps followed by 6 ns production at a temperature of 298 K and a pressure of 1 atm in the NpT ensemble using the Nosé-Hoover thermostat and barostat[76] with temperature and pressure damping parameters of 100 and 1,000 timesteps, respectively. A time step of 1 fs for bulk water and 0.25 fs for the confined system was employed throughout in conjunction with the SHAKE algorithm[54] only for the rigid water models. The spatial confinement was enforced for the confined water model using a cylindrical harmonic wall potential with a force constant of 5,000 kcal mol^{-1} $Å^{-2}$. The cylindrical axis of the water model was not confined and was subject to a pressure of 1 atm, resulting in a minor ~5% expansion in length on average after production dynamics.

Table 5.2.1 Parameters and reference dielectric constant of water models

Water Model	q_H (e)	qo (e)	σ_{OO} (Å)	ε_{OO} (kcal mol^{-1})	Dielectric constant
SPC/E	+0.4238	-0.8476	3.166	0.1554	71.0
SPC/Fw	+0.4100	- 0.8200	3.166	0.1554	79.6
TIP4P/ε	+0.5270	- 1.0540	3.165	0.1848	78.3

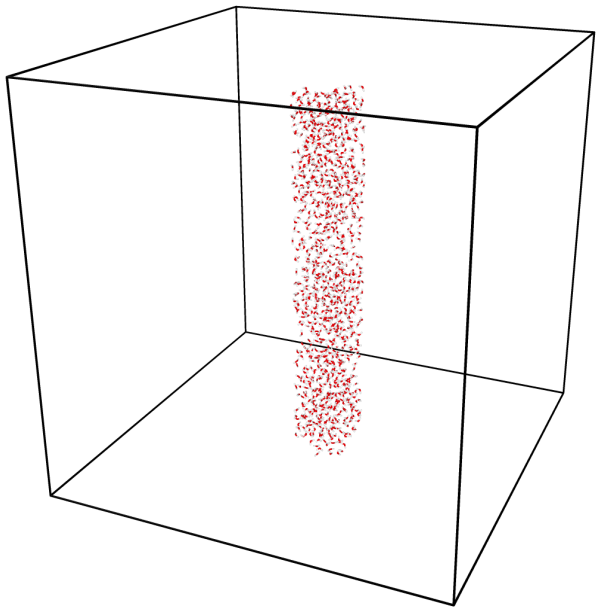

Fig. 5.2.1 Snapshot of starting configuration for molecular dynamics (MD) simulations, where water molecules are constrained by a cylindrical potential wall. The confined water channel is centered in the middle of a boundary unit box.

The dielectric constants of bulk and confined water models were computed using the PyLAT[77] package from the fluctuations of water dipole moments along the trajectories from the 6 ns of production dynamics according to:

$$\varepsilon = 1 + \frac{< M^2 > - < M >^2}{3\varepsilon_0 V k_B T}$$

where T is the absolute temperature, V is the volume of the solvent system, and M is the dipole moment of the solvent system.

Density functional theory (DFT) calculations were performed using Q-Chem 4.2[78] to estimate pK_a values and compute binding energies. The 3,5-dicarbamoylbenzoic acid and acetylated-piperazine (Ace-PIP) were selected as models of R-COOH and R_2-NH_2^+, respectively, present in the cross-linked polyamide network. All calculations were carried out using the dispersion-corrected, range-separated hybrid functional ωB97X-D[79] with the 6-311++G(d,p) basis set. All geometry optimizations were carried out in implicit solvent using the SMD solvation model[80]. The effect on pK_a of varying from low to higher dielectric was modeled with tetrahydrofuran (THF, ε=7.6), acetone (ε=20.7), acetonitrile (ε=37.5), dimethylsulfoxide (DMSO, ε=48.0), and water (ε=78.2). The pK_a values were calculated using a thermodynamic cycle approach, with the pK_a estimated as:

$$\mathrm{p}K_a = \frac{\Delta G}{2.303RT} = \frac{G_{HA} - G_A - G_{H^+}}{2.303RT}$$

$$\mathrm{p}K_a\left[\text{sub, correction}\right] = \mathrm{p}K_a\left[\text{sub, DFT}\right] + \mathrm{p}K_a\left[\text{ref, EXP}\right] - \mathrm{p}K_a\left[\text{ref, DFT}\right]$$

where entropic and zero-point energy contributions to the Gibbs free energies were obtained from an analytic Hessian calculation on the geometry optimized structure incorporating the relevant

implicit solvent model. We note that "sub" and "ref" denoted in the above equation abbreviate substrate and reference, respectively. The proton hydration free energies were taken from previous computational benchmarks[81]. To reduce sensitivity of computed pK_a values to both the solvent model and level of theory, we shifted all computed pK_a values by the difference of our computed pK_a values to available experimental data[82], [83] across several solvents of a related compound. For 3,5-dicarbamoylbenzoic acid, the reference compound chosen was benzoic acid, and for Ace-PIP, the reference was piperazine.

The binding enthalpy of Ace-PIP with a range of anions (i.e., ClO_4^-, ClO_3^-, NO_3^-, F^-, Cl^-, Br^-, I^-, and BO_2^-) was computed as:

$$\Delta H_{\text{binding}} = H_{\text{complex}} - H_{\text{Ace-PIP}} - H_{\text{ion}}$$

where the H refers to the zero-point vibrational energy-corrected electronic energy. The isolated Ace-PIP, anion, and anion-Ace-PIP complex were each geometry-optimized in implicit water solvent.

5.3 Results and discussion

MD simulations were used to assess the effect of nanoconfinement by a low permittivity media on the local dielectric constant of water. Several Lennard-Jones type water models (e.g., SPC/E, SPC/Fw, and TIP4P/ε) were used to simulate water dynamics in the bulk or under confinement. The reference calculated dielectric constants of bulk water range from roughly 71 to 79.6, which is in good agreement with its experimental value ($\varepsilon_{\text{water}}$ = 78.2) and validate our protocol for computing dielectric constants.

The simulation was allowed to reach steady-state conditions with 6 ns production, which is sufficient for an accurate determination of dielectric constant for various water models[84]. We calculated the dielectric constant from the fluctuation in the dipole moment along the MD trajectory. Testing on bulk SPC/E water comprising 64 to 5382 water molecules all yield converging results after 4 ns production run (Fig. 5.3.1), implying dielectric constants are relatively independent of system size. Under confinement, the surface-layer dielectric constant has been reported to decrease since the rotational degree of freedom of water are hindered in proximity to the surface. Inside a cylindrically shaped potential walls with a diameter of 2 nm, which is the most representative for the LIP membranes, we observe an evident decrease in the dielectric constant of water from its bulk value (Fig. 5.3.2), as the confined water molecules displayed a dielectric constant ~2-fold less than bulk water ($\varepsilon < 40$). These simulations support the ability of a low permittivity media, such as polyamide ($\varepsilon \approx 3$), to reduce the local dielectric constant of water upon extreme confinement.

However, in an extremely confined environment such as in sub-1 nm pore, the calculated dielectric constant can exceed the bulk value (Fig 5.3.2). The hydrogen bond networks are frustrated and presence of a potential wall indeed influences the molecular packing of fluids parallel to the surface. The calculated water density profile and parallel permittivity are reported to show anomalous pronounced peaks close to the interface with bulk-like regions in between[85], [86], and the resultant density profile is dependent on wall-fluid interactions (e.g. depth of carbon-water LJ potential well inside graphene slit-like channels[85]).

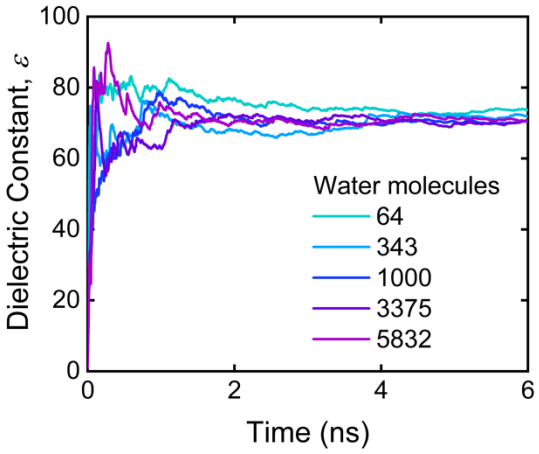

Fig. 5.3.1. Molecular dynamics simulations of the dielectric constant of bulk SPC/E water ranging from system sizes of 64 to 5832 water molecules.

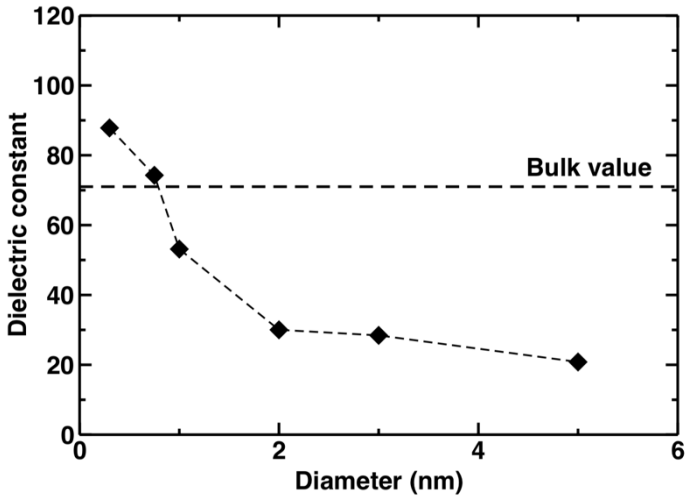

Fig. 5.3.2 Calculated dielectric constants of confined water in potential walls of diameter 1~5 nm.

DFT was then applied to evaluate the role of the intermediate dielectric constant in the ionization of semi-aromatic polyamide-based R-COOH. To reduce the complexity of modeling a highly cross-linked polymer network, we selected 3,5-dicarbamoylbenzoic acid as a truncated

molecular model of polyamide to study R-COOH ionization. This molecule is likely more representative of the polyamide-based R-COOH than a simple benzoic acid, as 3,5-dicarbamoylbenzoic acid possesses electron withdrawing carbonyl groups common to the polyamide chain. We modeled the ionization of our R-COOH analogue via DFT in solvents of varying dielectric constant and then corrected the calculated pK_a values based on experimental values of benzoic acid. We observed a notable increase in the corrected pK_a values of 3,5-dicarbamoylbenzoic acid experiencing lower dielectric constant, corroborating the viability of a dielectric-driven mechanism behind the upward-shift in R-COOH pK_a.

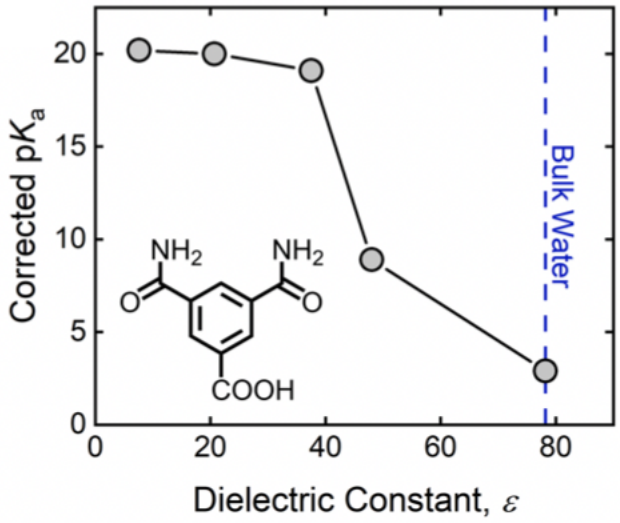

Fig 5.3.3 Relation between the pK_a of a polyamide-based R-COOH analogue (3,5-dicarbamoylbenzoic acid) and the dielectric constant of the surrounding media determined by density functional theory.

On the other hand, amine ionization in polyamide films is generally considered less important due to its low density relative to residual R-COOH. However, similar to R-COO$^-$, positively charged amine groups can impart hydrophilicity and influence electrostatic interactions between the membrane and charged constituents in the feed water. Therefore, it is

important to understand amine ionization when considering water and ion transport across nanoporous polyamide films. Previously, tungstate (WO_4^{2-}) was used as a probe to quantify ionized amine groups in fully-aromatic polyamide membranes, revealing a pK_a of ~4.1[87]. However, this result is not generalizable to all polyamide membranes. A pK_a of ~11 is more likely for the residual secondary amines (R_2-NH/R_2-NH_2^+) found in the PIP-based semi-aromatic polyamide membranes studied here[88].

To quantify R_2-NH_2^+ in our membranes, we employed DFT calculations to predict which monovalent anions expressed the most favorable binding. Binding favorability was quantified by the binding enthalpy (ΔH) between the anion and acetylated-piperazine (Ace-PIP), a truncated model of polyamide. Similar to R-COOH modeling, Ace-PIP was selected as the molecular analog for R_2-NH_2^+. DFT revealed metaborate (BO_2^-) binds the most favorably with Ace-PIP (Fig. 5.3.4); however, due to the tendencies of metaborate's conjugate acid to form metaboric acid, BO_2^- was considered unsuitable for quantifying R_2-NH_2^+ over a wide pH range. As such, bromide (Br^-) was selected as the most suitable counter-ion probe for assessing R_2-NH ionization.

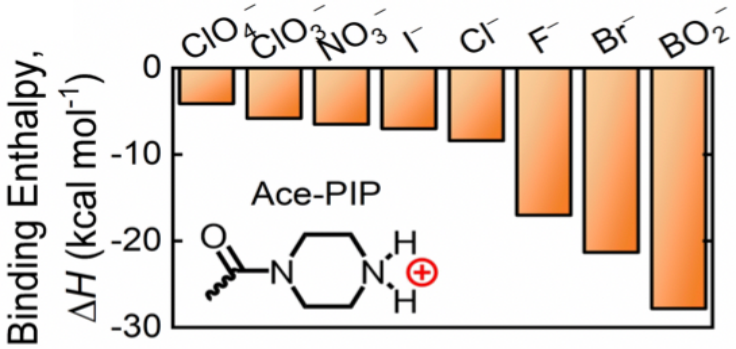

Fig. 5.3.4 Binding enthalpies between a polyamide-based piperazine analogue, acetylated-PIP (Ace-PIP), and probe anions gathered from DFT calculations.

Results from Fig. 5.3.5 imply that decrements to the local dielectric constant within the polyamide pore have negligible effect on the charge stability of R_2-NH_2^+. DFT calculations on the ionization of Ace-PIP in solvents of varying dielectric constant support this notion. Specifically, the projected increase (rather than a decrease) in the pK_a of Ace-PIP at lower dielectric constants indicates that lower permittivity media do not inhibit R_2-NH ionization. In other words, Ace-PIP can remain ionized over a wide pH range—regardless of its dielectric environment. This theoretical insight supports the experimental findings and reinforces the notion that R_2-NH ionization behavior for varying pH is similar across the film thickness, although the densities may vary.

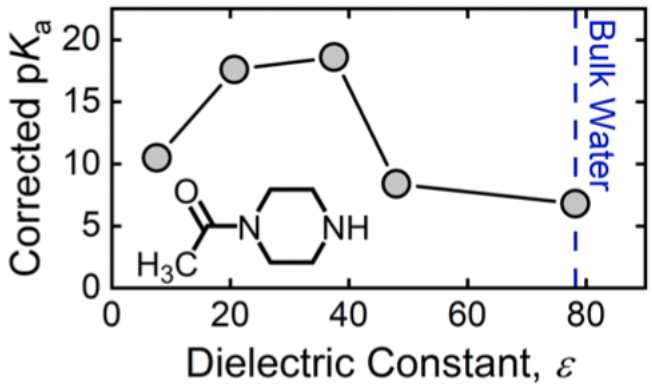

Fig. 5.3.5 Role of media dielectric constant, determined by DFT, on the pK_a of Ace-PIP.

5.4 Conclusion

In this study, we assessed the ionization behavior of nanoporous polyamide selective layers in nanofiltration membranes. Classical molecular dynamics combined with first-principles

simulations support a dielectric-driven mechanism of location-dependent ionization of carboxyl groups in polyamide membranes. Within membrane pores, nanoconfinement of water effectively decreases its local permittivity, thus changing the ionization behavior of carboxyl groups due to reduced charge stability, measured by enhancements in its pK_a. On the other hand, amine ionization behaves invariably across the membrane. These findings highlight the influence of nanoconfinement on membrane permselectivity and provide fundamental understandings of ionization for novel membrane design.

References

[1] W. Sparreboom, A. van den Berg, and J. C. T. Eijkel, “Principles and applications of nanofluidic transport,” *Nat. Nanotechnol.*, vol. 4, no. 11, pp. 713–720, Nov. 2009, doi: 10.1038/nnano.2009.332.

[2] J. C. T. Eijkel and A. van den Berg, “Nanofluidics: what is it and what can we expect from it?,” *Microfluid. Nanofluidics*, vol. 1, no. 3, pp. 249–267, Jul. 2005, doi: 10.1007/s10404-004-0012-9.

[3] N. R. Tas, P. Mela, T. Kramer, J. W. Berenschot, and A. van den Berg, “Capillarity Induced Negative Pressure of Water Plugs in Nanochannels,” *Nano Lett.*, vol. 3, no. 11, pp. 1537–1540, Nov. 2003, doi: 10.1021/nl034676e.

[4] G. Hummer, J. C. Rasaiah, and J. P. Noworyta, “Water conduction through the hydrophobic channel of a carbon nanotube,” *Nature*, vol. 414, no. 6860, pp. 188–190, Nov. 2001, doi: 10.1038/35102535.

[5] D. Stein, M. Kruithof, and C. Dekker, “Surface-Charge-Governed Ion Transport in Nanofluidic Channels,” *Phys. Rev. Lett.*, vol. 93, no. 3, Jul. 2004, doi: 10.1103/PhysRevLett.93.035901.

[6] C. Duan, W. Wang, and Q. Xie, “Review article: Fabrication of nanofluidic devices,” *Biomicrofluidics*, vol. 7, no. 2, p. 026501, Mar. 2013, doi: 10.1063/1.4794973.

[7] C. Vieu *et al.*, “Electron beam lithography: resolution limits and applications,” *Appl. Surf. Sci.*, vol. 164, no. 1–4, pp. 111–117, Sep. 2000, doi: 10.1016/S0169-4332(00)00352-4.

[8] T. Liu, C. Burger, and B. Chu, “Nanofabrication in polymer matrices,” *Prog. Polym. Sci.*, vol. 28, no. 1, pp. 5–26, Jan. 2003, doi: 10.1016/S0079-6700(02)00077-1.

[9] C. K. Jeong *et al.*, “Electrical Biomolecule Detection Using Nanopatterned Silicon via Block Copolymer Lithography,” *Small*, vol. 10, no. 2, pp. 337–343, Jan. 2014, doi: 10.1002/smll.201301202.

[10] P. Abgrall and N. T. Nguyen, “Nanofluidic Devices and Their Applications,” *Anal. Chem.*, vol. 80, no. 7, pp. 2326–2341, Apr. 2008, doi: 10.1021/ac702296u.

[11] C. Cottin-Bizonne, B. Cross, A. Steinberger, and E. Charlaix, “Boundary Slip on Smooth Hydrophobic Surfaces: Intrinsic Effects and Possible Artifacts,” *Phys. Rev. Lett.*, vol. 94, no. 5, Feb. 2005, doi: 10.1103/PhysRevLett.94.056102.

[12] W. R. Bowen and A. W. Mohammad, “Characterization and Prediction of Nanofiltration Membrane Performance—A General Assessment,” *Chem. Eng. Res. Des.*, vol. 76, no. 8, pp. 885–893, Nov. 1998, doi: 10.1205/026387698525685.

[13] F. Zhu, E. Tajkhorshid, and K. Schulten, “Theory and Simulation of Water Permeation in Aquaporin-1,” *Biophys. J.*, vol. 86, no. 1, pp. 50–57, Jan. 2004, doi: 10.1016/S0006-3495(04)74082-5.

[14] P. Nednoor, N. Chopra, V. Gavalas, L. G. Bachas, and B. J. Hinds, “Reversible Biochemical Switching of Ionic Transport through Aligned Carbon Nanotube Membranes,” *Chem. Mater.*, vol. 17, no. 14, pp. 3595–3599, Jul. 2005, doi: 10.1021/cm047844s.

[15] R. Karnik, R. Fan, M. Yue, D. Li, P. Yang, and A. Majumdar, “Electrostatic Control of Ions and Molecules in Nanofluidic Transistors,” *Nano Lett.*, vol. 5, no. 5, pp. 943–948, May 2005, doi: 10.1021/nl050493b.

[16] P. Pang, J. He, J. H. Park, P. S. Krstić, and S. Lindsay, “Origin of Giant Ionic Currents in Carbon Nanotube Channels,” *ACS Nano*, vol. 5, no. 9, pp. 7277–7283, Sep. 2011, doi: 10.1021/nn202115s.
[17] R. G. Parr, “Density Functional Theory of Atoms and Molecules,” in *Horizons of Quantum Chemistry*, K. Fukui and B. Pullman, Eds. Dordrecht: Springer Netherlands, 1980, pp. 5–15.
[18] K. Burke, “Perspective on density functional theory,” *J. Chem. Phys.*, vol. 136, no. 15, p. 150901, Apr. 2012, doi: 10.1063/1.4704546.
[19] L. Versluis and T. Ziegler, “The determination of molecular structures by density functional theory. The evaluation of analytical energy gradients by numerical integration,” *J. Chem. Phys.*, vol. 88, no. 1, pp. 322–328, Jan. 1988, doi: 10.1063/1.454603.
[20] M. W. Wong, “Vibrational frequency prediction using density functional theory,” *Chem. Phys. Lett.*, vol. 256, no. 4–5, pp. 391–399, Jul. 1996, doi: 10.1016/0009-2614(96)00483-6.
[21] V. M. L. dos Santos, J. A. B. da Silva, L. Stragevitch, and R. L. Longo, “Thermochemistry of biodiesel oxidation reactions: A DFT study,” *Fuel*, vol. 90, no. 2, pp. 811–817, Feb. 2011, doi: 10.1016/j.fuel.2010.09.017.
[22] Y. Wang, X. Gong, and J. Wang, “Comparative DFT study of structure and magnetism of TMnOm (TM = Sc–Mn, n = 1–2, m = 1–6) Clusters,” *Phys. Chem. Chem. Phys.*, vol. 12, no. 10, p. 2471, 2010, doi: 10.1039/b920033a.
[23] H. C. Andersen, “Molecular dynamics simulations at constant pressure and/or temperature,” *J. Chem. Phys.*, vol. 72, no. 4, pp. 2384–2393, Feb. 1980, doi: 10.1063/1.439486.
[24] M. Matsumoto, S. Saito, and I. Ohmine, “Molecular dynamics simulation of the ice nucleation and growth process leading to water freezing,” *Nature*, vol. 416, no. 6879, pp. 409–413, Mar. 2002, doi: 10.1038/416409a.
[25] W. Jiang and B. Roux, “Free Energy Perturbation Hamiltonian Replica-Exchange Molecular Dynamics (FEP/H-REMD) for Absolute Ligand Binding Free Energy Calculations,” *J. Chem. Theory Comput.*, vol. 6, no. 9, pp. 2559–2565, Sep. 2010, doi: 10.1021/ct1001768.
[26] D. R. Hartree, “The Wave Mechanics of an Atom with a Non-Coulomb Central Field. Part II. Some Results and Discussion,” *Math. Proc. Camb. Philos. Soc.*, vol. 24, no. 1, pp. 111–132, Jan. 1928, doi: 10.1017/S0305004100011920.
[27] L. H. Thomas, “The calculation of atomic fields,” *Math. Proc. Camb. Philos. Soc.*, vol. 23, no. 5, pp. 542–548, Jan. 1927, doi: 10.1017/S0305004100011683.
[28] P. Hohenberg and W. Kohn, “Inhomogeneous Electron Gas,” *Phys. Rev.*, vol. 136, no. 3B, pp. B864–B871, Nov. 1964, doi: 10.1103/PhysRev.136.B864.
[29] W. Kohn and L. J. Sham, “Self-Consistent Equations Including Exchange and Correlation Effects,” *Phys. Rev.*, vol. 140, no. 4A, pp. A1133–A1138, Nov. 1965, doi: 10.1103/PhysRev.140.A1133.
[30] D. M. Ceperley and B. J. Alder, “Ground State of the Electron Gas by a Stochastic Method,” *Phys. Rev. Lett.*, vol. 45, no. 7, pp. 566–569, Aug. 1980, doi: 10.1103/PhysRevLett.45.566.
[31] S. Krüger, S. Vent, and N. Rösch, “Size dependence of bond length and binding energy in palladium and gold clusters,” *Berichte Bunsenges. Für Phys. Chem.*, vol. 101, no. 11, pp. 1640–1643, Nov. 1997, doi: 10.1002/bbpc.19971011115.

[32] Y. Zhang and W. Yang, “A challenge for density functionals: Self-interaction error increases for systems with a noninteger number of electrons,” *J. Chem. Phys.*, vol. 109, no. 7, pp. 2604–2608, Aug. 1998, doi: 10.1063/1.476859.
[33] J. P. Perdew *et al.*, “Atoms, molecules, solids, and surfaces: Applications of the generalized gradient approximation for exchange and correlation,” *Phys. Rev. B*, vol. 46, no. 11, pp. 6671–6687, Sep. 1992, doi: 10.1103/PhysRevB.46.6671.
[34] S. Plimpton, “Fast Parallel Algorithms for Short-Range Molecular Dynamics,” *J. Comput. Phys.*, vol. 117, no. 1, pp. 1–19, Mar. 1995, doi: 10.1006/jcph.1995.1039.
[35] A. J. Haslam, D. Moldovan, V. Yamakov, D. Wolf, S. R. Phillpot, and H. Gleiter, “Stress-enhanced grain growth in a nanocrystalline material by molecular-dynamics simulation,” *Acta Mater.*, vol. 51, no. 7, pp. 2097–2112, Apr. 2003, doi: 10.1016/S1359-6454(03)00011-9.
[36] M. Karplus and J. Kuriyan, “Molecular dynamics and protein function,” *Proc. Natl. Acad. Sci.*, vol. 102, no. 19, pp. 6679–6685, May 2005, doi: 10.1073/pnas.0408930102.
[37] J. A. Maier, C. Martinez, K. Kasavajhala, L. Wickstrom, K. E. Hauser, and C. Simmerling, “ff14SB: Improving the Accuracy of Protein Side Chain and Backbone Parameters from ff99SB,” *J. Chem. Theory Comput.*, vol. 11, no. 8, pp. 3696–3713, Aug. 2015, doi: 10.1021/acs.jctc.5b00255.
[38] A. D. MacKerell *et al.*, “All-Atom Empirical Potential for Molecular Modeling and Dynamics Studies of Proteins †,” *J. Phys. Chem. B*, vol. 102, no. 18, pp. 3586–3616, Apr. 1998, doi: 10.1021/jp973084f.
[39] W. L. Jorgensen and J. Tirado-Rives, “The OPLS [optimized potentials for liquid simulations] potential functions for proteins, energy minimizations for crystals of cyclic peptides and crambin,” *J. Am. Chem. Soc.*, vol. 110, no. 6, pp. 1657–1666, Mar. 1988, doi: 10.1021/ja00214a001.
[40] G. Lamoureux, A. D. MacKerell, and B. Roux, “A simple polarizable model of water based on classical Drude oscillators,” *J. Chem. Phys.*, vol. 119, no. 10, pp. 5185–5197, Sep. 2003, doi: 10.1063/1.1598191.
[41] P. T. Kiss and A. Baranyai, “A systematic development of a polarizable potential of water,” *J. Chem. Phys.*, vol. 138, no. 20, p. 204507, May 2013, doi: 10.1063/1.4807600.
[42] Steinczinger, “Comparison of the TIP4P-2005, SWM4-DP and BK3 interaction potentials of liquid water with respect to their consistency with neutron and X-ray diffraction data of pure water,” *Condens. Matter Phys.*, vol. 16, no. 4, p. 43604, 2013, doi: 10.5488/CMP.16.43604.
[43] J. R. Pliego, Jr. and J. M. Riveros, “A Theoretical Analysis of the Free-Energy Profile of the Different Pathways in the Alkaline Hydrolysis of Methyl Formate In Aqueous Solution,” *Chem. - Eur. J.*, vol. 8, no. 8, p. 1945, Apr. 2002, doi: 10.1002/1521-3765(20020415)8:8<1945::AID-CHEM1945>3.0.CO;2-T.
[44] G. M. Torrie and J. P. Valleau, “Nonphysical sampling distributions in Monte Carlo free-energy estimation: Umbrella sampling,” *J. Comput. Phys.*, vol. 23, no. 2, pp. 187–199, Feb. 1977, doi: 10.1016/0021-9991(77)90121-8.
[45] A. Barducci, M. Bonomi, and M. Parrinello, “Metadynamics,” *WIREs Comput. Mol. Sci.*, vol. 1, no. 5, pp. 826–843, Sep. 2011, doi: 10.1002/wcms.31.

[46] S. Kumar, J. M. Rosenberg, D. Bouzida, R. H. Swendsen, and P. A. Kollman, “THE weighted histogram analysis method for free-energy calculations on biomolecules. I. The method,” *J. Comput. Chem.*, vol. 13, no. 8, pp. 1011–1021, Oct. 1992, doi: 10.1002/jcc.540130812.

[47] C. H. Bennett, “Efficient estimation of free energy differences from Monte Carlo data,” *J. Comput. Phys.*, vol. 22, no. 2, pp. 245–268, Oct. 1976, doi: 10.1016/0021-9991(76)90078-4.

[48] M. R. Shirts and J. D. Chodera, “Statistically optimal analysis of samples from multiple equilibrium states,” *J. Chem. Phys.*, vol. 129, no. 12, p. 124105, Sep. 2008, doi: 10.1063/1.2978177.

[49] P. Li, X. Jia, X. Pan, Y. Shao, and Y. Mei, “Accelerated Computation of Free Energy Profile at ab Initio Quantum Mechanical/Molecular Mechanics Accuracy via a Semi-Empirical Reference Potential. I. Weighted Thermodynamics Perturbation,” *J. Chem. Theory Comput.*, vol. 14, no. 11, pp. 5583–5596, Nov. 2018, doi: 10.1021/acs.jctc.8b00571.

[50] L. Martínez, R. Andrade, E. G. Birgin, and J. M. Martínez, “PACKMOL: A package for building initial configurations for molecular dynamics simulations,” *J. Comput. Chem.*, vol. 30, no. 13, pp. 2157–2164, Oct. 2009, doi: 10.1002/jcc.21224.

[51] K. Szalewicz, “Symmetry-adapted perturbation theory of intermolecular forces: Symmetry-adapted perturbation theory,” *Wiley Interdiscip. Rev. Comput. Mol. Sci.*, vol. 2, no. 2, pp. 254–272, Mar. 2012, doi: 10.1002/wcms.86.

[52] G. Lamoureux and B. Roux, “Modeling induced polarization with classical Drude oscillators: Theory and molecular dynamics simulation algorithm,” *J. Chem. Phys.*, vol. 119, no. 6, pp. 3025–3039, Aug. 2003, doi: 10.1063/1.1589749.

[53] S. Nosé, “A unified formulation of the constant temperature molecular dynamics methods,” *J. Chem. Phys.*, vol. 81, no. 1, pp. 511–519, Jul. 1984, doi: 10.1063/1.447334.

[54] J.-P. Ryckaert, G. Ciccotti, and H. J. . Berendsen, “Numerical integration of the cartesian equations of motion of a system with constraints: molecular dynamics of n-alkanes,” *J. Comput. Phys.*, vol. 23, no. 3, pp. 327–341, Mar. 1977, doi: 10.1016/0021-9991(77)90098-5.

[55] H. J. C. Berendsen, J. R. Grigera, and T. P. Straatsma, “The missing term in effective pair potentials,” *J. Phys. Chem.*, vol. 91, no. 24, pp. 6269–6271, Nov. 1987, doi: 10.1021/j100308a038.

[56] I. S. Ufimtsev and T. J. Martinez, “Quantum Chemistry on Graphical Processing Units. 3. Analytical Energy Gradients, Geometry Optimization, and First Principles Molecular Dynamics,” *J. Chem. Theory Comput.*, vol. 5, no. 10, pp. 2619–2628, Oct. 2009, doi: 10.1021/ct9003004.

[57] *D.A. Case, V. Babin, J.T. Berryman, R.M. Betz, Q. Cai, D.S. Cerutti, T.E. Cheatham, III, T.A. Darden, R.E. Duke, H. Gohlke, A.W. Goetz, S. Gusarov, N. Homeyer, P. Janowski, J. Kaus, I. Kolossváry, A. Kovalenko, T.S. Lee, S. LeGrand, T. Luchko, R. Luo, B. Madej, K.M. Merz, F. Paesani, D.R. Roe, A. Roitberg, C. Sagui, R. Salomon-Ferrer, G. Seabra, C.L. Simmerling, W. Smith, J. Swails, R.C. Walker, J. Wang, R.M. Wolf, X. Wu and P.A. Kollman (2014), AMBER 14, University of California, San Francisco.* .

[58] M. A. Rohrdanz, K. M. Martins, and J. M. Herbert, “A long-range-corrected density functional that performs well for both ground-state properties and time-dependent density functional theory excitation energies, including charge-transfer excited states,” *J. Chem. Phys.*, vol. 130, no. 5, p. 054112, Feb. 2009, doi: 10.1063/1.3073302.

[59] W. L. Jorgensen, J. Chandrasekhar, J. D. Madura, R. W. Impey, and M. L. Klein, "Comparison of simple potential functions for simulating liquid water," *J. Chem. Phys.*, vol. 79, no. 2, pp. 926–935, Jul. 1983, doi: 10.1063/1.445869.
[60] T. M. Parker, L. A. Burns, R. M. Parrish, A. G. Ryno, and C. D. Sherrill, "Levels of symmetry adapted perturbation theory (SAPT). I. Efficiency and performance for interaction energies," *J. Chem. Phys.*, vol. 140, no. 9, p. 094106, Mar. 2014, doi: 10.1063/1.4867135.
[61] P. V. Klimovich, M. R. Shirts, and D. L. Mobley, "Guidelines for the analysis of free energy calculations," *J. Comput. Aided Mol. Des.*, vol. 29, no. 5, pp. 397–411, May 2015, doi: 10.1007/s10822-015-9840-9.
[62] C. Lee, W. Yang, and R. G. Parr, "Development of the Colle-Salvetti correlation-energy formula into a functional of the electron density," *Phys. Rev. B*, vol. 37, no. 2, pp. 785–789, Jan. 1988, doi: 10.1103/PhysRevB.37.785.
[63] S. Grimme, J. Antony, S. Ehrlich, and H. Krieg, "A consistent and accurate *ab initio* parametrization of density functional dispersion correction (DFT-D) for the 94 elements H-Pu," *J. Chem. Phys.*, vol. 132, no. 15, p. 154104, Apr. 2010, doi: 10.1063/1.3382344.
[64] M. P. Allen and D. J. Tildesley, *Computer simulation of liquids*. 2017.
[65] W. Humphrey, A. Dalke, and K. Schulten, "VMD: Visual molecular dynamics," *J. Mol. Graph.*, vol. 14, no. 1, pp. 33–38, Feb. 1996, doi: 10.1016/0263-7855(96)00018-5.
[66] F. Neese, "The ORCA program system," *WIREs Comput. Mol. Sci.*, vol. 2, no. 1, pp. 73–78, Jan. 2012, doi: 10.1002/wcms.81.
[67] T. Z. H. Gani and H. J. Kulik, "Where Does the Density Localize? Convergent Behavior for Global Hybrids, Range Separation, and DFT+U," *J. Chem. Theory Comput.*, vol. 12, no. 12, pp. 5931–5945, Dec. 2016, doi: 10.1021/acs.jctc.6b00937.
[68] F. Banhart, J. Kotakoski, and A. V. Krasheninnikov, "Structural Defects in Graphene," *ACS Nano*, vol. 5, no. 1, pp. 26–41, Jan. 2011, doi: 10.1021/nn102598m.
[69] D. Sen, R. Thapa, and K. K. Chattopadhyay, "Small Pd cluster adsorbed double vacancy defect graphene sheet for hydrogen storage: A first-principles study," *Int. J. Hydrog. Energy*, vol. 38, no. 7, pp. 3041–3049, Mar. 2013, doi: 10.1016/j.ijhydene.2012.12.113.
[70] N. Ghaderi and M. Peressi, "First-Principle Study of Hydroxyl Functional Groups on Pristine, Defected Graphene, and Graphene Epoxide," *J. Phys. Chem. C*, vol. 114, no. 49, pp. 21625–21630, Dec. 2010, doi: 10.1021/jp108688m.
[71] M. Elimelech and W. A. Phillip, "The Future of Seawater Desalination: Energy, Technology, and the Environment," *Science*, vol. 333, no. 6043, pp. 712–717, Aug. 2011, doi: 10.1126/science.1200488.
[72] J. R. Werber, C. O. Osuji, and M. Elimelech, "Materials for next-generation desalination and water purification membranes," *Nat. Rev. Mater.*, vol. 1, no. 5, May 2016, doi: 10.1038/natrevmats.2016.18.
[73] D. Chen, J. R. Werber, X. Zhao, and M. Elimelech, "A facile method to quantify the carboxyl group areal density in the active layer of polyamide thin-film composite membranes," *J. Membr. Sci.*, vol. 534, pp. 100–108, Jul. 2017, doi: 10.1016/j.memsci.2017.04.001.
[74] R. Fuentes-Azcatl and M. C. Barbosa, "Thermodynamic and dynamic anomalous behavior in the TIP4P/ε water model," *Phys. Stat. Mech. Its Appl.*, vol. 444, pp. 86–94, Feb. 2016, doi: 10.1016/j.physa.2015.10.027.

[75] Y. Wu, H. L. Tepper, and G. A. Voth, “Flexible simple point-charge water model with improved liquid-state properties,” *J. Chem. Phys.*, vol. 124, no. 2, p. 024503, Jan. 2006, doi: 10.1063/1.2136877.

[76] M. E. Tuckerman, Y. Liu, G. Ciccotti, and G. J. Martyna, “Non-Hamiltonian molecular dynamics: Generalizing Hamiltonian phase space principles to non-Hamiltonian systems,” *J. Chem. Phys.*, vol. 115, no. 4, pp. 1678–1702, Jul. 2001, doi: 10.1063/1.1378321.

[77] M. T. Humbert, Y. Zhang, and E. J. Maginn, “PyLAT: Python LAMMPS Analysis Tools,” *J. Chem. Inf. Model.*, vol. 59, no. 4, pp. 1301–1305, Apr. 2019, doi: 10.1021/acs.jcim.9b00066.

[78] Y. Shao *et al.*, “Advances in molecular quantum chemistry contained in the Q-Chem 4 program package,” *Mol. Phys.*, vol. 113, no. 2, pp. 184–215, Jan. 2015, doi: 10.1080/00268976.2014.952696.

[79] J.-D. Chai and M. Head-Gordon, “Long-range corrected hybrid density functionals with damped atom–atom dispersion corrections,” *Phys. Chem. Chem. Phys.*, vol. 10, no. 44, p. 6615, 2008, doi: 10.1039/b810189b.

[80] A. V. Marenich, C. J. Cramer, and D. G. Truhlar, “Universal Solvation Model Based on Solute Electron Density and on a Continuum Model of the Solvent Defined by the Bulk Dielectric Constant and Atomic Surface Tensions,” *J. Phys. Chem. B*, vol. 113, no. 18, pp. 6378–6396, May 2009, doi: 10.1021/jp810292n.

[81] I. A. Topol, G. J. Tawa, S. K. Burt, and A. A. Rashin, “Calculation of Absolute and Relative Acidities of Substituted Imidazoles in Aqueous Solvent,” *J. Phys. Chem. A*, vol. 101, no. 51, pp. 10075–10081, Dec. 1997, doi: 10.1021/jp9723168.

[82] A. Kütt *et al.*, “pKa values in organic chemistry – Making maximum use of the available data,” *Tetrahedron Lett.*, vol. 59, no. 42, pp. 3738–3748, Oct. 2018, doi: 10.1016/j.tetlet.2018.08.054.

[83] F. Khalili, A. Henni, and A. L. L. East, “p K_a Values of Some Piperazines at (298, 303, 313, and 323) K,” *J. Chem. Eng. Data*, vol. 54, no. 10, pp. 2914–2917, Oct. 2009, doi: 10.1021/je900005c.

[84] O. Gereben and L. Pusztai, “On the accurate calculation of the dielectric constant from molecular dynamics simulations: The case of SPC/E and SWM4-DP water,” *Chem. Phys. Lett.*, vol. 507, no. 1–3, pp. 80–83, Apr. 2011, doi: 10.1016/j.cplett.2011.02.064.

[85] M. H. Motevaselian, S. Y. Mashayak, and N. R. Aluru, “Extended coarse-grained dipole model for polar liquids: Application to bulk and confined water,” *Phys. Rev. E*, vol. 98, no. 5, Nov. 2018, doi: 10.1103/PhysRevE.98.052135.

[86] C. Schaaf and S. Gekle, “Spatially resolved dielectric constant of confined water and its connection to the non-local nature of bulk water,” *J. Chem. Phys.*, vol. 145, no. 8, p. 084901, Aug. 2016, doi: 10.1063/1.4960775.

[87] O. Coronell, M. I. González, B. J. Mariñas, and D. G. Cahill, “Ionization Behavior, Stoichiometry of Association, and Accessibility of Functional Groups in the Active Layers of Reverse Osmosis and Nanofiltration Membranes,” *Environ. Sci. Technol.*, vol. 44, no. 17, pp. 6808–6814, Sep. 2010, doi: 10.1021/es100891r.

[88] H. K. Hall, “Correlation of the Base Strengths of Amines [1],” *J. Am. Chem. Soc.*, vol. 79, no. 20, pp. 5441–5444, Oct. 1957, doi: 10.1021/ja01577a030.